Master Thesis

Jülich Centre for Neutron Science 2 (JCNS-2)

RWTH Aachen University

Dynamic Magnetic Structural Properties of FeO_x Nanoparticles as Dispersion

First Examiner: Prof. Dr. Karen Friese (JCNS-2)

Second Examiner: Prof. Dr. Regina Dittmann (PGI-7)

Supervisor: PD Dr. Oleg Petracic and Dr. Asmaa Qdemat (both JCNS-2)

Submitted by: Yiyu Lin

Study Program: Master in Materials Science

Matriculation Number: 416449

Submission Date: 02.06.2025

Eidesstattliche Versicherung
Declaration of Academic Integrity

_____   _____
Name, Vorname/Last Name, First Name   Matrikelnummer (freiwillige Angabe)
                                             Student ID Number (optional)

Ich versichere hiermit an Eides Statt, dass ich die vorliegende Arbeit/Bachelorarbeit/
Masterarbeit* mit dem Titel
I hereby declare under penalty of perjury that I have completed the present paper/bachelor's thesis/master's thesis* entitled

_____

_____

_____

selbstständig und ohne unzulässige fremde Hilfe (insbes. akademisches Ghostwriting) erbracht habe. Ich habe keine anderen als die angegebenen Quellen und Hilfsmittel benutzt; dies umfasst insbesondere auch Software und Dienste zur Sprach-, Text- und Medienproduktion. Ich erkläre, dass für den Fall, dass die Arbeit in unterschiedlichen Formen eingereicht wird (z.B. elektronisch, gedruckt, geplottet, auf einem Datenträger) alle eingereichten Versionen vollständig übereinstimmen. Die Arbeit hat in gleicher oder ähnlicher Form noch keiner Prüfungsbehörde vorgelegen.

independently and without unauthorized assistance from third parties (in particular academic ghostwriting. I have not used any other sources or aids than those indicated; this includes in particular software and services for language, text, and media production. In the event that the work is submitted in different formats (e.g. electronically, printed, plotted, on a data carrier), I declare that all the submitted versions are fully identical. I have not previously submitted this work, either in the same or a similar form to an examination body.

_____   _____
Ort, Datum/City, Date   Unterschrift/Signature

                                             *Nichtzutreffendes bitte streichen/Please delete as appropriate

Belehrung:
Official Notification:

§ 156 StGB: Falsche Versicherung an Eides Statt
Wer vor einer zur Abnahme einer Versicherung an Eides Statt zuständigen Behörde eine solche Versicherung falsch abgibt oder unter Berufung auf eine solche Versicherung falsch aussagt, wird mit Freiheitsstrafe bis zu drei Jahren oder mit Geldstrafe bestraft.
§ 156 StGB (German Criminal Code): False Unsworn Declarations
Whosoever before a public authority competent to administer unsworn declarations (including Declarations of Academic Integrity) falsely submits such a declaration or falsely testifies while referring to such a declaration shall be liable to imprisonment for a term not exceeding three years or to a fine.
§ 161 StGB: Fahrlässiger Falscheid; fahrlässige falsche Versicherung an Eides Statt
(1) Wenn eine der in den §§ 154 bis 156 bezeichneten Handlungen aus Fahrlässigkeit begangen worden ist, so tritt Freiheitsstrafe bis zu einem Jahr oder Geldstrafe ein.
(2) Straflosigkeit tritt ein, wenn der Täter die falsche Angabe rechtzeitig berichtigt. Die Vorschriften des § 158 Abs. 2 und 3 gelten entsprechend.
§ 161 StGB (German Criminal Code): False Unsworn Declarations Due to Negligence
(1) If an individual commits one of the offenses listed in §§ 154 to 156 due to negligence, they are liable to imprisonment for a term not exceeding one year or to a fine.
(2) The offender shall be exempt from liability if they correct their false testimony in time. The provisions of § 158 (2) and (3) shall apply accordingly.

Die vorstehende Belehrung habe ich zur Kenntnis genommen:
I have read and understood the above official notification:

_____   _____
Ort, Datum/City, Date   Unterschrift/Signature

Abstract

Magnetic nanoparticles (MNPs) possess distinctive size-dependent magnetic behaviors and structural responses that are critically influenced by their surrounding media. Among them, FeOx nanoparticles are of particular interest due to their high chemical stability and tunable magnetic properties, making them suitable candidates for applications ranging from magnetic sensing to biomedical imaging and nanorheology. In this study, the dynamic magnetic and structural properties of 15 nm FeOx nanoparticle dispersions are systematically investigated under varying external magnetic fields and solvent viscosities.

Magnetic characterizations were conducted using a superconducting quantum interference device (SQUID) magnetometer and a physical property measurement system (PPMS). Hysteresis loops, zero-field-cooled/field-cooled (ZFC/FC) magnetization, AC susceptibility, and time-dependent relaxation measurements were used to identify the blocking temperature and distinguish between Néel and Brownian relaxation mechanisms. Structural analysis was performed through small-angle X-ray scattering (SAXS) and dynamic light scattering (DLS), with SAXS measurements carried out both in zero field and under applied magnetic fields.

The results reveal that solvent viscosity significantly affects the relaxation behavior and that Brownian relaxation becomes dominant at high temperatures, particularly in low-viscosity solvents. Under applied magnetic fields, SAXS data show clear anisotropic scattering patterns, indicating field-induced particle assembly. Classical polydisperse sphere and sticky hard sphere (SHS) models were employed to fit the SAXS data, allowing extraction of core radii, interaction strength parameters, and evidence of magnetic field–induced aggregation.

Overall, this work provides detailed insight into how the magnetic and structural dynamics of MNPs are coupled through solvent-mediated interactions and external fields. These findings contribute to the fundamental understanding of magnetically responsive nanoparticle systems and lay the groundwork for designing advanced MNP-based materials for biomedical and soft-matter applications.

Zusammenfassung

Magnetische Nanopartikel (MNPs) zeigen ausgeprägte größenabhängige magnetische Eigenschaften und strukturelle Anordnungen, die stark vom umgebenden Medium beeinflusst werden. Unter ihnen sind FeOx-Nanopartikel besonders interessant aufgrund ihrer hohen chemischen Stabilität und anpassbaren magnetischen Eigenschaften, was sie zu vielversprechenden Kandidaten für Anwendungen von der magnetischen Sensorik bis hin zur biomedizinischen Bildgebung und Nanorheologie macht. In dieser Arbeit werden die dynamischen magnetischen und strukturellen Eigenschaften von 15 nm großen FeOx-Nanopartikeldispersionen systematisch unter verschiedenen externen Magnetfeldern und Lösungsmittelviskositäten untersucht.

Die magnetischen Eigenschaften wurden mit einem SQUID-Magnetometer (Superconducting Quantum Interference Device) und einem Physical Property Measurement System (PPMS) charakterisiert. Hystereseschleifen, Zero-Field-Cooled/Field-Cooled (ZFC/FC)-Magnetisierung, AC-Suszeptibilität sowie zeitabhängige Relaxationsmessungen wurden verwendet, um die Blockierungstemperatur zu bestimmen und zwischen Néel- und Brown'scher Relaxation zu unterscheiden. Die strukturelle Analyse erfolgte mittels Kleinwinkel-Röntgenstreuung (SAXS) und dynamischer Lichtstreuung (DLS), wobei SAXS-Messungen sowohl ohne als auch mit angelegtem Magnetfeld durchgeführt wurden.

Die Ergebnisse zeigen, dass die Viskosität des Lösungsmittels das Relaxationsverhalten deutlich beeinflusst und dass die Brown'sche Relaxation bei hohen Temperaturen, insbesondere in niederviskosen Lösungsmitteln, dominiert. Unter Magnetfeldeinfluss zeigen die SAXS-Daten deutliche anisotrope Streumuster, was auf eine feldinduzierte Partikelanordnung hinweist. Klassische Modelle wie das polydisperse Kugelmodell und das Sticky-Hard-Sphere-Modell (SHS) wurden verwendet, um die SAXS-Daten zu analysieren, wobei Parameter wie Kernradius, Wechselwirkungsstärke und Hinweise auf feldinduzierte Aggregation gewonnen wurden.

Insgesamt bietet diese Arbeit einen detaillierten Einblick in die Kopplung der magnetischen und strukturellen Dynamiken von magnetischen Nanopartikeln durch lö-

sungsmittelvermittelte Wechselwirkungen und externe Felder. Diese Erkenntnisse tragen zum grundlegenden Verständnis magnetisch ansprechbarer Nanopartikelsysteme bei und bilden eine Grundlage für die Entwicklung fortschrittlicher, MNP-basierter Materialien für biomedizinische und weiche Materie-Anwendungen.

Contents

1 Introduction

1.1 Background

"Why can't we write the entire 24 volumes of the Encyclopedia Britannica on the head of a pin?"

—— Richard Phillips Feynman

This question comes from one of Richard Feynman's famous lectures titled "There's Plenty of Room at the Bottom", delivered at the annual meeting of the American Physical Society in 1959. The words of Feynman attracted the interest of many scientists and brought them into the field of nanoscience and nanotechnology. Much like the branches of a tree, research on nanoscience and nanotechnology has expanded to encompass nearly every scientific discipline over the past few decades, including physics, chemistry, biology, and electrical engineering (figure 1.1).

The prefix 'nano' is derived from the Greek word 'nanos', meaning 'dwarf', and refers to objects beeing extremely small. While the concept of nanoscale has become familiar in recent years, humanity's earliest utilization of nanoscience and nanotechnology dates back to the fourth century AD with the creation of the Lycurgus Cup, made from dichroic glass. This dichroic glass is a colloid dispersion of gold and silver nanoparticles with a size from 50 to 100 nanometers. The nanoscale effect produces a green color in reflected light and a red color in transmitted light [1]. Nowadays, an increasing number of nanomaterials and nanoproducts are integrated into daily life, including nanoparticle catalysts, nanoelectronic devices, and contrast agents of magnetic resonance imaging (MRI) [2].

Among these applications, magnetic nanoparticles (MNPs) have attracted significant research attention due to their exclusive properties, such as a high surface-area-to-
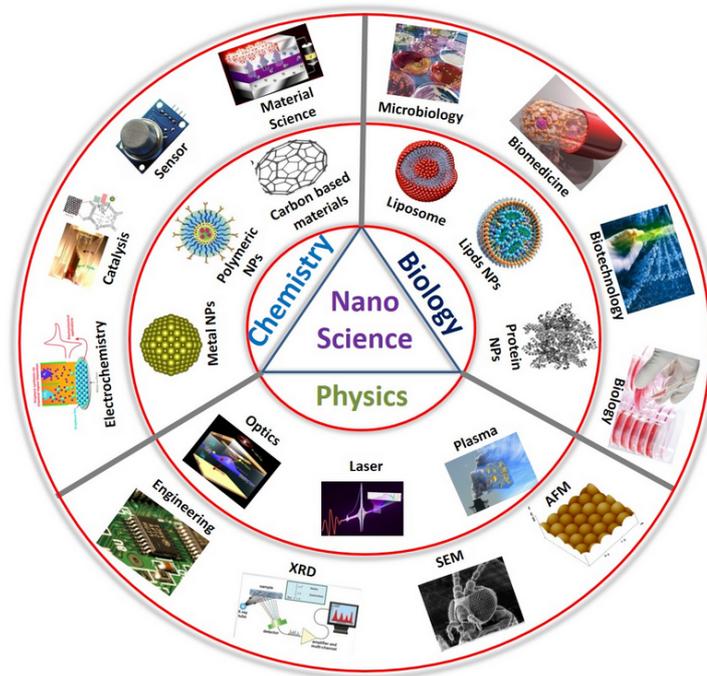
Figure 1.1: Applications of nanoscience and nanotechnology [1]

volume ratio and size-dependent magnetic behavior [3]. A lot of studies have focused on the properties of MNPs. For example, M. Modestino *et al.* compared the interaction of Fe$_3$O$_4$ MNPs in DC and AC magnetic fields, and found that the temperature associated with the peak in AC susceptibility follows different interaction mechanisms at low and high temperatures [4]. Md Ehsan Sadat investigated the effect of dipole interactions on Fe$_3$O$_4$ MNPs, and observed that the blocking temperature increases with stronger interactions, while the Brownian relaxation peak shifts to lower frequencies by increasing magnetic concentration [5]. Jonathon C. Davidson *et al.* developed an analytic approximation for the Brownian relaxation time of single domain MNPs in an external field, derived an expression validated against formulas and simulation results [6].

However, the properties of MNPs system depend not only on the nanoparticles themselves but also on their surrounding environment, especially the viscosity of the solvent [7]. Eric Roeben *et al.* investigated the susceptibility of CoFe$_2$O$_4$ nanoparticles in solvents with different viscosities and compared the microscopic results with the values, which were calculated using the Gemant-DiMarzio-Bishop approach [8]. They concluded that the bias in values obtained from this approach depends on particle concentration and the size ratio of particles to solvent molecules [8]. Melissa Hess *et al.* studied the rotational dynamics of the spherical CoFe$_2$O$_4$ nanoparticles

in aqueous polymer solutions of polyethylene glycol (PEG). Their results demonstrated that nanorheological measurements correspond to macroscopic rheology as long as the solution is unentangled and the particles are larger than the polymer chains [9]. Chinmoy Saayujya *et al.* directly probed the relaxation behavior of FeOx superparamagnetic nanoparticles in water and glycerol by pulsed magnetic field relaxometry and found a strong linear relationship between relaxation time constant and viscosity in a certain regime [10].

1.2 Motivation

As mentioned above, many researchers have focused on the dynamic behavior of magnetic nanoparticles, and this project is motivated by the same interest.

For a single-domain magnetic particle suspended in a liquid, in addition to random Brownian motion, the particle can align its magnetic moment with the direction of an applied magnetic field through either internal or physical rotation. This process is known as magnetic relaxation, which includes Néel relaxation (internal rotation) and Brownian relaxation (physical rotation). Néel relaxation involves the magnetic moment overcoming the energy barrier imposed by magnetic anisotropy, while Brownian relaxation requires the physical rotation of the entire particle against the viscous resistance of the surrounding solvent. Macroscopically, this resistance is described by the solvent's viscosity, which quantifies the friction arising from relative motion between components within the fluid system. Additionally, external magnetic fields can also introduce structural changes in the dispersion due to the self-assembly of magnetic nanoparticles, transforming from dispersed particles to chains, columns, or network-like structures [11, 12].

Therefore, this work investigates the magnetic and structural properties of FeOx nanoparticle dispersions under an applied magnetic field. Understanding the magnetic relaxation and structural transformations of MNPs is crucial, as these dynamic behaviors directly impact their performance in various applications, particularly in biomedical science. Elucidating these mechanisms allows for a deeper understanding of magnetic interactions and enables more flexible and efficient use of MNPs. Moreover, this study examines the influence of solvents with different viscosities on the dynamic behavior of MNPs. Based on existing theoretical models, the relationship between the dynamic magnetic response and the internal mechanical properties

of the system (viscosity) has been studied briefly. This provides a foundation for developing novel characterization methods of magnetic properties.

1.3 Overview

Basic magnetic properties, such as hysteresis loop and magnetic behavior by zero field cooling and field cooling, and magnetic relaxation behavior of MNPs are studied by superconducting quantum interference device (SQUID) magnetometry, while AC susceptibility of MNPs is studied by the physical properties measurement system (PPMS). The size and structure of MNPs are measured by the small-angle X-ray scattering (SAXS) technique with and without a magnetic field and the dynamic light scattering (DLS) technique.

This thesis is organized into five chapters:

Chapter 1 introduces the background and motivation of the study, emphasizing the importance of magnetic nanoparticles (MNPs) and their dynamic behavior in different dispersion environments.

Chapter 2 presents the theoretical foundations, including fundamental magnetism, relaxation mechanisms, and structural models used for data analysis.

Chapter 3 details the magnetic characterization of FeO_x nanoparticle dispersions using SQUID and PPMS systems, focusing on hysteresis, blocking behavior, and relaxation dynamics.

Chapter 4 discusses the structural analysis of nanoparticle dispersions with and without external magnetic fields using SAXS and DLS techniques, and evaluates interparticle interactions through structure factor modeling.

Chapter 5 and chapter 6 summarize the key findings and offer conclusions and future perspectives regarding the coupled magnetic–structural behavior of FeO_x nanoparticles in fluid systems.

2 Theoretical Background

2.1 Magnetism

Magnetism is a fundamental physical property of materials that arises from electrons, particularly their spin and orbital motion. The magnetic properties of solids can be observed as paramagnetism, diamagnetism and various types of magnetic long-range order. Moreover, magnetic anisotropy often plays an important role. This section will introduce these concepts and how they are modified at the nanoscale.

2.1.1 Diamagnetism and Paramagnetism

All types of materials respond to an external magnetic field. In the case of absent long-range order, either diamagnetism or paramagnetism is encountered. Diamagnetism represents an antiparallel alignment to the direction of the magnetic field, while paramagnetism is characterized by a parallel alignment of magnetic moments.

Diamagnetism

In addition to the electron spin, the orbital motion of the electrons around the nucleus also contributes to the magnetic behaviour. The physical mechanism of diamagnetism needs to be described via Quantum Mechanics [13]. It leads to an effective opposite alignment of the magnetic moment relative to the applied field (Figure 2.1 left, $\chi < 0$).

Paramagnetism

Paramagnetism is caused by unpaired electrons in materials. Each electron has a magnetic moment due to its spin. Unpaired electrons lead to a non-zero net magnetic moment of the material. However, thermal fluctuations cause the orientations of magnetic moments to be randomly aligned. The competition between the alignment of moments due to the field and the dis-alignment due to thermal fluctuations results in a net positive magnetic susceptibility (Figure 2.1, $\chi > 0$) [13].
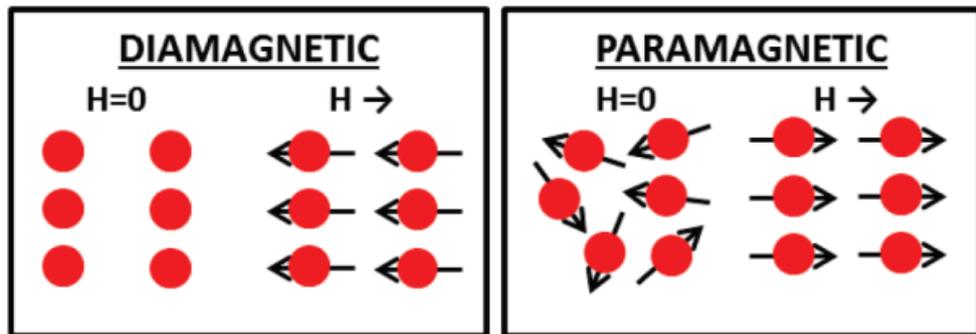

Figure 2.1: Diamagnetism and paramagnetism [14]

2.1.2 Magnetic Orders

Interactions between magnetic moments can lead to long-range order, e.g., ferromagnetism, antiferromagnetism, or ferrimagnetism. In the following subsections these terms will be discussed.

Ferromagnetism

The magnetic moments of a ferromagnetic system are aligned parallel to each other, so that the net moment is non-zero. This results in a spontaneous magnetisation of the system even in the absence of a field. One finds a phase transition from ferromagnetism to paramagnetism when the thermal energy is high enough, i.e., when the critical temperature (Curie temperature) is reached. The Curie-Weiss law (Equation 2.1) describes the relationship between the magnetic susceptibility and

the temperature of a ferromagnetic system above the Curie temperature.

$$\chi = \frac{C}{T - T_C} \tag{2.1}$$

Where χ is susceptibility, C is the Curie constant, T is temperature and T_C is the Curie temperature.

Ferromagnetic order can be affected not only by thermal fluctuations but also by an external field. A magnetic field parallel to the magnetic moments enhances the magnetization up to a maximum value called saturation magnetization. A magnetic field antiparallel to the magnetic moments reduces the magnetization and eventually reverses the orientation of the moments. The field required for this reversal is known as the coercive field. Even after the external field is removed, the material can retain some magnetization, known as residual magnetization (remanent magnetization).

Antiferromagnetism

The magnetic moments in an antiferromagnetic system are antiparallel to the nearest neighbour moments. Hence, the net moment is zero, resulting in zero magnetization without an applied field. As with the ferromagnetic system, there is a critical temperature for the transition from antiferromagnetism to paramagnetism due to thermal fluctuations, called the Néel temperature. The magnetic susceptibility and temperature relation (equation A.1) of an antiferromagnetic system is similar to that of a ferromagnetic system above the Néel temperature.

$$\chi = \frac{C}{T + T_N} \tag{2.2}$$

Where T_N is the Néel temperature.

Antiferromagnetic order can be considered to be composed of two sublattices with the same magnetization but opposite orientation.

Ferrimagnetism

The alignment of the magnetic moments of the ferrimagnetic system is similar to that of an antiferromagnetic system with the difference that the net moments of

the sublattices have not equal magnetization and hence do not compensate to zero. The overall net behaviour hence resembles that of a ferromagnet. Because ferrimagnetism depends particularly on the crystal structure, the magnetic susceptibility and the temperature behavior of the sublattices, a ferrimagnetic system has a more complicated temperature dependence than a ferromagnetic or antiferromagnetic system.
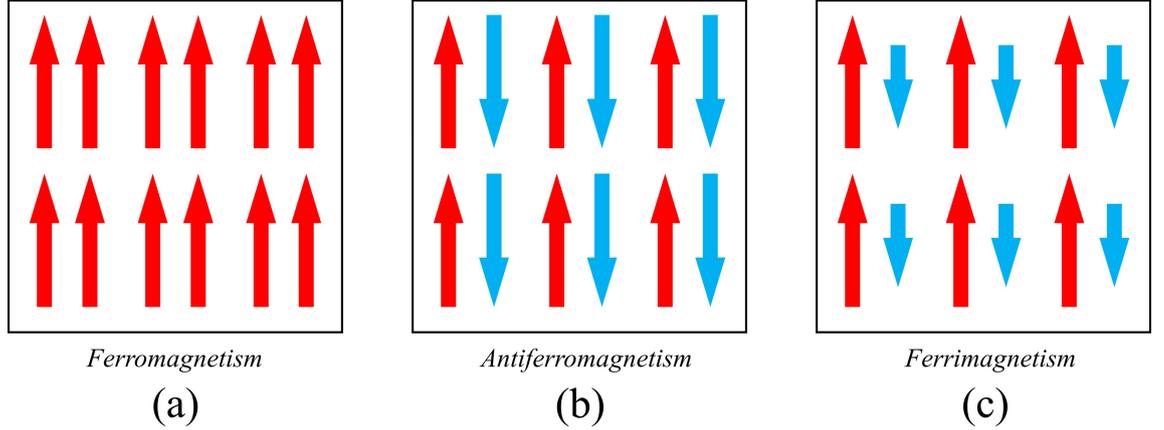

| Ferromagnetism | Antiferromagnetism | Ferrimagnetism |
| (a) | (b) | (c) |

Figure 2.2: (a) Ferromagnetism (b) Antiferromagnetism (c) Ferrimagnetism

2.1.3 Magnetic Interactions

The magnetic order discussed in the previous section is determined by the interactions between magnetic moments. The most relevant types of interactions can be divided into dipolar and exchange interactions.

2.1.3.1 Dipolar interaction

Similar to interacting electric dipoles, two magnetic dipole moments (magnetic moments) have a classical long-range interaction. The energy of this interaction can be described as follows

$$E_{dd} = \frac{\mu_0}{4\pi r^3} \left[\vec{\mu}_1 \cdot \vec{\mu}_2 - \frac{3}{r^2} (\vec{\mu}_1 \cdot \vec{r})(\vec{\mu}_2 \cdot \vec{r}) \right] \tag{2.3}$$

Where E_{dd} is the dipolar interaction energy, $\mu_0 = 4\pi * 10^{-7} H m^{-1}$ is the vacuum permeability, r is the distance between the two dipoles, $\vec{\mu}_1$ and $\vec{\mu}_2$ are the magnetic moments of the two dipoles respectively.

Assuming that the dipoles have moments of the order of the Bohr magneton μ_B and are separated on the nanometre scale, the magnetic dipolar interaction energy and the thermal energy are of the same order of magnitude at a few Kelvin, which means that the dipolar interaction is negligible for magnetic ordering in bulk materials. Therefore, the exchange interaction dominates in this case.

Exchange interaction

Exchange interactions are a consequence of the quantum mechanical "exchange" of electrons between neighbouring orbitals. They can be divided into the following types.

Direct exchange interaction, which occurs between magnetic atoms that are close enough together to allow the electron to hop directly from one atom to another without an intermediary.

Indirect exchange interaction, which occurs between magnetic ions and non-magnetic intermediates such as oxygen ions O^{2-}. There are two types of interaction:

Super exchange interaction: Electrons from non-magnetic ions hop to magnetic ions around the non-magnetic ion, resulting in antiferromagnetism or ferrimagnetism.

Double exchange interaction: Electrons from non-magnetic ions hop to magnetic ions with different valence states (Mn^{3+} and Mn^{4+}) around this ion, resulting in ferromagnetism according to Hund's rule.

RKKY exchange interaction: Conduction electrons can be polarized by localised magnetic ions, which in turn leads to an indirect coupling of the localised magnetic ions. The result can be antiferromagnetism or ferromagnetism because the exchange integral has a cosine-type oscillating term with distance.

$$J_{RKKY} \propto \frac{cos\ 2k_F r}{r^3} \tag{2.4}$$

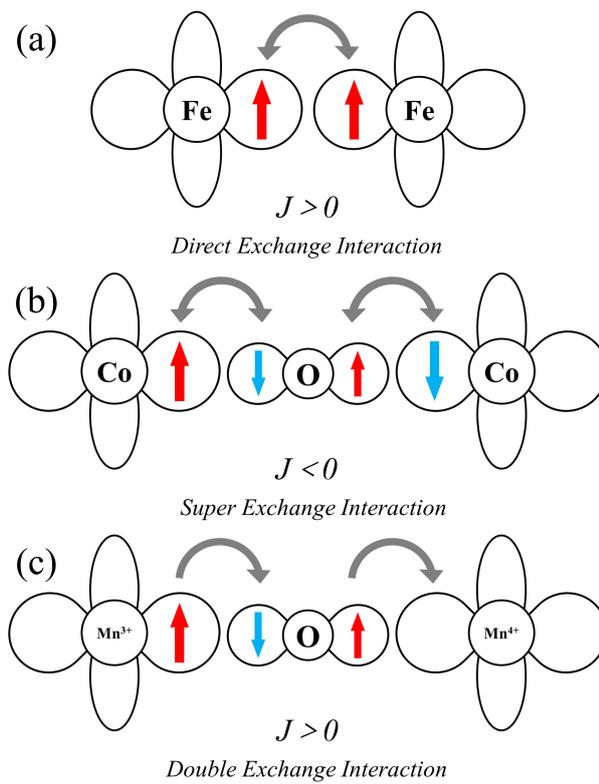Where r is the distance and k_F is the radius of the Fermi surface.

Figure 2.3: (a) Direct interaction (b) Super exchange interaction (c) Double exchange interaction, inspired by [15]

2.1.4 Magnetic Anisotropy

Often in magnetic materials, there is one preferred direction of the spontaneous magnetization, called the easy magnetic axis. In contrast, another direction, called the hard magnetic axis, costs additional energy. This phenomenon, where magnetic moments have different tendencies to orient in different directions, is known as magnetic anisotropy. The energy of magnetic anisotropy can be described as follows:

$$E_a = KV sin^2\theta \tag{2.5}$$

Where E_a is the magnetic anisotropy energy, K is the anisotropy constant, V is the volume of material, and θ is the angle between magnetization and magnetic easy axis. For a magnetic nanoparticle system, the magnetic anisotropy is mainly caused by shape and surface effects.

Shape effect is the result of demagnetization fields. The energy of the demagnetization field can be described as follows:

$$E_d = -\frac{\mu_0}{2} \int \vec{M} \cdot \vec{H_{dm}} dV \tag{2.6}$$

Where E_d is the demagnetization energy, μ_0 is the vacuum permeability, M is the magnetization and V is the volume of material, and $\vec{H_{dm}} = \vec{N} \cdot \vec{M}$ is the induced demagnetization field with N called demagnetization factor, which depends on the shape of material, for example, $N = \frac{1}{3}$ for a spherical body. Hence it has no shape anisotropy, because the contribution of demagnetization is the same in every direction. As for an ellipsoidal body, the anisotropy energy is as follows:

$$E_{shape} = \frac{1}{2}\mu_0 V (N_x M_x^2 + N_y M_y^2 + N_z M_z^2) \tag{2.7}$$

x, y, z correspond to three axes, and the demagnetization factor has a relation as follows:

$$N_x + N_y + N_z = 1 \tag{2.8}$$

Surface effects are the result of the different atomic coordination at the surfaces of a system. The surface effect can be described as follows:

$$K_{eff} = K_V + \frac{S}{V}K_S = K_V + \frac{6}{d}K_S \tag{2.9}$$

Where K_{eff} is the effective surface anisotropy, K_V is volume anisotropy, K_S is the surface anisotropy and $\frac{S}{V}$ is the ratio of surface and volume with $S = \pi d^2$ and $V = \frac{\pi d^3}{6}$, d is the diameter of particle.

2.2 Magnetic Nanoparticles

The magnetic properties of materials introduced in the last section are found in bulk materials. However, many effects change significantly at the nanoscale, such as in magnetic nanoparticles studied in this project. For example, iron oxide nanoparticles in the 10nm size range are superparamagnetic at room temperature, while magnetite (Fe_3O_4) is fully magnetized in bulk [16].

2.2.1 Finite Size Effects of Nanoparticles

The properties of materials, e.g., magnetic properties, change with size scaling when entering the nanometre range. A summary of the finite size effects in magnetic nanoparticles can be found in Ref. [17]:

1. **Reduction of magnetization and saturation magnetization**: With size scaling, the proportion of surface atoms increases. However, compared to the atoms inside the particles, the surface atoms have lower coordination and weaker exchange interactions, resulting in a deviation of the surface order from the internal order, e.g., a tilted or disordered structure;

2. **Enhancement of magnetic anisotropy energy**: Lower coordination of surface atoms induces not only surface disorder but also broken local symmetry on the surface, while defects and lattice distortions usually appear on the surface. Both surface effects lead to an increased anisotropy constant K;

3. **Transition of superparamagnetism**: When a magnetic particle is smaller than a critical value (10~100 nm usually), it prefers to stay in a single domain state due to the higher energy cost of the domain wall [18], which means that a nanoparticle could be seen as a magnetic dipole with one magnetic

moment. Therefore, a system of dispersed magnetic nanoparticles can exhibit superparamagnetism;

4. **Collective states due to interactions**: The dipolar interaction between nanoparticles becomes more effective with larger particle density. These interactions can lead to various collective magnetic behaviours;

2.2.2 Energy of Magnetic Nanoparticles

The Stoner-Wohlfarth model describes the magnetic behavior of single magnetic nanoparticles or interacting magnetic nanoparticles. This model divides the total energy (E) of the system into four contributions [18]:

$$E = E_J + E_K + E_H + E_d = -J\sum_{i,j} \vec{S_i} \cdot \vec{S_j} - K\sum_i (\vec{k_i} \cdot \vec{S_i})^2 - g\mu_b\mu_0 \sum_i \vec{H} \cdot \vec{S_i}$$
$$+ \frac{g\mu_b\mu_0}{4\pi\vec{r_{ij}}^3} \sum_{i,j} (\vec{S_i} \cdot \vec{S_j} - \frac{\vec{S_i} \cdot \vec{r_{ij}} - \vec{S_j} \cdot \vec{r_{ij}}}{\vec{r_{ij}}^2}) \quad (2.10)$$

Where E is the total energy, E_J, E_K, E_H and E_d correspond to the exchange energy, anisotropy energy, Zeeman energy with applied field, and dipolar energy, respectively. J is the exchange interaction constant, $\vec{S_i}$ and $\vec{S_j}$ are spin vectors of two spins (magnetic moments), K is the anisotropy constant, $\vec{k}$ is anisotropy axis vector, g is the relevant g-factor, μ_b is Bohr magneton, μ_0 is vacuum permeability, $\vec{H}$ is the applied field and $\vec{r}$ is the distance between two spins.

It is known that fragmenting moments into domains by introducing a domain wall can minimize the energy of the stray field. However, if the energy cost of domain formation is greater than the energy reduction of the stray field, the magnetic moments prefer to remain in the single domain state. For a spherical particle, there is a critical radius estimated by the equation 2.11, below which magnetic particles are considered to be single-domain particles or 'superspins', with magnetic moments in the order of thousands of Bohr magnetons.

$$R_c = \frac{36\sqrt{AK}}{\mu_0 M_s^2} \quad (2.11)$$

13

Where $A \propto J$ is the 'exchange stiffness' and M_s is the saturation magnetization. Hence, according to the Stoner-Wohlfarth model, the energy of one magnetic particle is described as follows:

$$E_{np} = -K_{eff}V(\vec{k} \cdot \vec{m}_{np})^2 - \mu_0 M_s V \vec{H} \cdot \vec{m}_{np} \tag{2.12}$$

Where E_{np} is the total energy of single particle, K_{eff} is the effective anisotropy constant, V is the volume of the nanoparticle and $\vec{m}_{np}$ is the unit vector of magnetization direction. Considering the dipolar interactions only, the energy of a particle in the system can be described as follows [18]:

$$E_i = -K_iV_i(\vec{k} \cdot \vec{m}_i)^2 - \mu_0 M_s V_i \vec{H} \cdot \vec{m}_i + \frac{\mu_0 M_s^2}{4\pi \vec{r_{ij}}^3} \sum_i V_iV_j(\vec{m}_i \cdot \vec{m}_j - \frac{\vec{m}_i \cdot \vec{r}_{ij} - \vec{m}_j \cdot \vec{r}_{ij}}{\vec{r_{ij}}^2})$$
$$\tag{2.13}$$

Where E_i the total energy of particle with index i in the system, K_i is the anisotropy constant, $V_{i,j}$ is the volume, M_s is the saturation magnetization, $\vec{m_{i,j}}$ and $\vec{r_{i,j}}$ are the unit vectors of the direction of magnetization and the location of the particle, respectively. The equation 2.13 shows the most relevant interactions in the nanoparticle dispersion system.

2.2.3 Magnetic States of Nanoparticle Systems

As the interaction strength between magnetic nanoparticles increases, the system can exhibit several different magnetic states. These states can be classified by the relaxation time (τ), which characterises the time it takes for the moments to align with the external magnetic field, and are expressed as follows [19, 20]:

(I) Independent states with none or weak interaction:

- *Superparamagnetic state (SPM)*: Nanoparticles behave independently, with negligible interactions between them. The magnetic moments are random and disordered, and their orientation changes stochastically. The relaxation time shows Nèel-Brown (Nèel-Arrhenius) relation:

$$\tau = \tau_0 \, exp(\frac{KV}{k_B T}) \tag{2.14}$$

where τ is the relaxation time, τ_0 is the attempt time (usually $10^{-9} \sim 10^{-12}$ s), K is the anisotropy constant, V is the volume of nanoparticle, k_B is the Boltzmann constant and T is the temperature;

- *Modified superparamagnetic state*: The individual behaviour is similar to the SPM state, but the energy barrier $\triangle E^*$ contains the anisotropy energy and the effective interactions between nanoparticles, and hence the relaxation time is modified:

$$\tau = \tau_0 \ exp(\frac{\triangle E^*}{k_B T}) \tag{2.15}$$

(II) Collective states with strong interaction:

- *Glass-like freezing state*: The system transitions from independent to collective behaviour with higher interactions between nanoparticles. The relaxation time shows a Vogel-Fulcher relationship with the glass temperature T_0:

$$\tau = \tau_0 \ exp(\frac{\triangle E^*}{k_B(T - T_0)}) \tag{2.16}$$

- *Superspin glass state (SSG)*: The collective behaviour with stronger interaction is similar to that of a spin glass. The magnetic moments are aligned in seemingly random directions, while a collective overall state is found characterised by a spectrum of relaxation times covering an infinitely large range of time scales. The superspins transform into the spin glass phase below the spin glass transition temperature T_g, the relaxation time:

$$\tau = \tau_0 \ (\frac{T - T_g}{T_g})^{-zv} \tag{2.17}$$

where zv is the critical exponent;

- *Superferromagnetic state (SFM)*: collective behaviour with even stronger interactions, so that the magnetic moments are ordered. The superspins exhibit a ferromagnetic-like phase below a critical temperature T_c, and the relaxation time is:

$$\tau = \tau_0 \ (\frac{T - T_c}{T_c})^{-zv} \tag{2.18}$$

It can be assumed that a magnetic nanoparticle system will only remain in one of three magnetic states, as shown below:

- *Superparamagnetism (SPM) state*: none or negligible inter-particles interaction, nanoparticles rotate individually, corresponding to SPM or modified SPM states;

- *Superspin glass (SSG) state*: interparticle interaction, nanoparticles transform into a collective state (superspin glass) below the glass temperature T_g, corresponding to the SSG state;

- *Superferromagnetic (SFM) state*: strong interparticle interactions, nanoparticles transform into a collective state (superferromagnetism) below the critical temperature T_c, corresponding to the SFM state;

2.2.4 Phase Diagram of Magnetic Nanoparticles

As discussed above, the collective magnetic states of a dispersed magnetic nanoparticle system depend on the strength of the interactions between the particles. Figure 2.4 shows the magnetic state phase diagram, where the x axis represents the interaction strength between nanoparticles, or simply considered as the concentration, while the y axis represents the temperature.

Three transition lines are visible in the phase diagram: (i) the Curie temperature $T_{c,bulk}$, (ii) the spin glass temperature T_g or critical temperature T_c, and (iii) the blocking temperature T_b. Below $T_{c,bulk}$, the magnetic order within the nanoparticle becomes ferromagnetic, but there is no order between the particles. Thus, the whole system exhibits superparamagnetism by viewing the nanoparticles as individual magnetic moments. This is the so-called superparamagnetic (SPM) phase. T_g and T_c separate the superspin glass (SSG) and superferromagnetism (SFM) phases from the SPM phase. The entire system shows SSG or SFM behaviour when cooled below the corresponding critical temperatures.

Note that T_b depends not only on the relaxation of the nanoparticles, but also on the characteristic time τ_m of the measurement, which ranges from 100 to $10^{-8}s$. If the characteristic time is longer than the relaxation time of the nanoparticles, the nanoparticles show superparamagnetism. On the other hand, if the characteris-
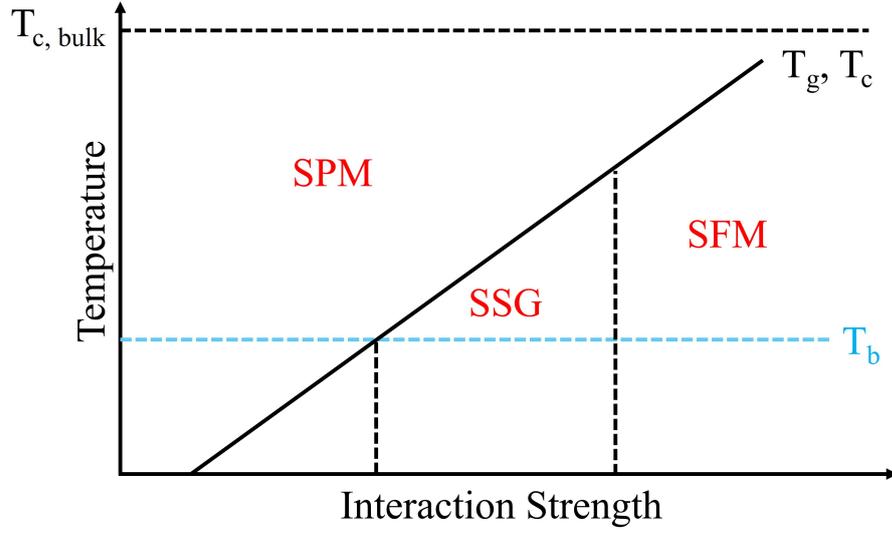
Figure 2.4: Magnetic phase diagram, inspired from [21]

tic time is shorter than the relaxation time of the nanoparticles, the nanoparticles are considered to be in a 'blocked' magnetic state, which means that the magnetic moments rotate very slowly and appear as static during the measurement. One can estimate the blocking temperature T_b of single domain nanoparticles in $100s$ characteristic time by the equation [22]:

$$T_b = \frac{KV_0}{25k_B} \qquad (2.19)$$

Where K is the anisotropy constant and V_0 is the volume of a nanoparticle. Once cooled below the blocking temperature, collective order can be 'masked' by the magnetically blocked state [23].

2.2.5 Relaxation of Magnetic Nanoparticles

There are two relaxation mechanisms of magnetic nanoparticles for their alignment, Néel and Brownian relaxation. Néel relaxation is a rotation of the internal magnetic moment within the nanoparticles without any relative motion between the particles and the solvent, whereas Brownian relaxation is a physical rotation of the entire nanoparticles with relative motion between the particles and the solvent.

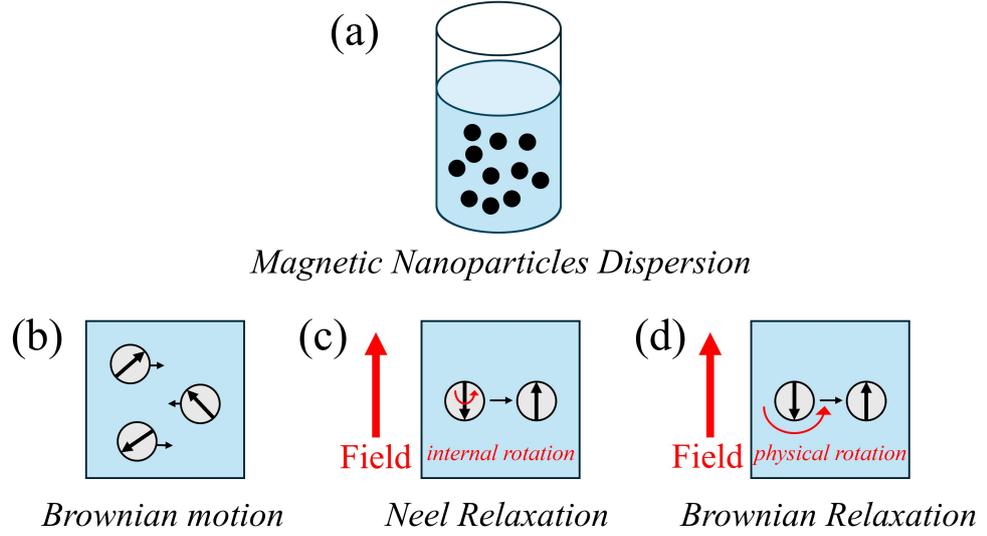The Néel relaxation time is described as follows [24]:

Figure 2.5: (a) Nanoparticles dispersion (b) Brownian motion (c) Neel relaxation (d) Brownian relaxation

$$\tau_N = \tau_0 \; exp(\frac{KV}{k_B T}) \tag{2.20}$$

Where τ_N is the Néel relaxation time and τ_0 is the attempt time. This expression demonstrates that magnetic anisotropy energy is the main energy barrier for Néel relaxation.

The Brownian relaxation time is described as follows [24]:

$$\tau_B = \frac{3\eta V_H}{k_B T} \tag{2.21}$$

Where τ_B is the Brownian relaxation time, η is the viscosity of the solvent, and V_H is the hydrodynamic volume of nanoparticles. This expression shows that the rheological friction between particles and solvent is the main barrier to Brownian relaxation.

Since these two relaxations can appear at the same time, one has to consider an effective relaxation time as follows [25]:

$$\frac{1}{\tau_{eff}} = \frac{1}{\tau_B} + \frac{1}{\tau_B} \tag{2.22}$$

However, when the solvent is frozen, the magnetic nanoparticles remain in a solid environment. Therefore, it can be assumed that there is no Brownian relaxation

due to a very large rheological friction. In other words, at low temperatures below the melting point of the solvent, only the Néel relaxation needs to be considered.

2.3 Scattering

Scattering is a powerful tool for investigating how particles or waves interact with matter and is widely used to probe the structure, size, and dynamics of materials. By analyzing the scattering pattern of the outgoing waves from a sample, information can be obtained from the atomic to the nanoscale. For nanoparticle systems, techniques such as X-ray, electron, or neutron scattering provide insight into particle size, shape, arrangement, and interparticle interactions. Scattering intensity is essential for studying the evolution of complex systems.
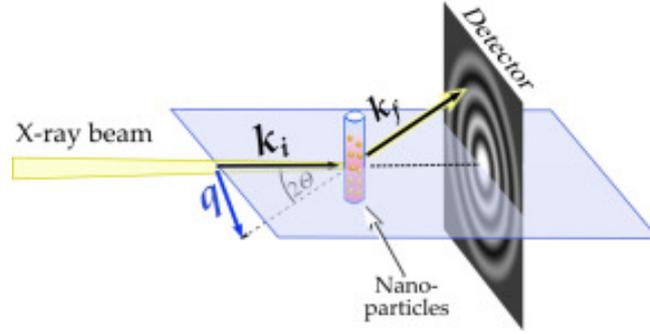
2.3.1 Principle of Scattering

Figure 2.6: Principle of X-ray scattering [26]

When a wave hits a particular material, it interacts with the material. In the case of X-rays, the interaction primarily occurs with the electrons. Then the wave is scattered in several directions and shows as an interference pattern at the detector. Thus the scattering vector $\vec{q}$ is the subtraction between the scattering vector $\vec{k}_s$ ($\vec{k}_f$ in figure 2.6) and the incidence vector $\vec{k}_i$ of the x-ray and is described as [27]:

$$\vec{q} = \vec{k}_s - \vec{k}_i \tag{2.23}$$

$$q = |\vec{q}| = \frac{4\pi}{\lambda} sin\theta \tag{2.24}$$

Where $\vec{k}_s$ and $\vec{k}_i$ are the wave vectors of the scattering X-ray and incident X-ray, respectively.

The scattering amplitude $A(\vec{q})$ is defined as the Fourier transformed electron density

or scattering length density (SLD) $\rho(\vec{r})$, i.e., $\mathcal{F}(\rho(\vec{r}))$:

$$A(\vec{q}) = \mathcal{F}(\rho(\vec{r})) = \int \rho(\vec{r}) e^{-i\vec{q}\cdot\vec{r}} d^3\vec{r} \tag{2.25}$$

Then, the scattering intensity $I(\vec{q})$ is the square of the scattering amplitude $|A(\vec{q})|^2$:

$$I(\vec{q}) = |A(\vec{q})|^2 = \left| \int \rho(r) e^{-i\vec{q}\cdot\vec{r}} d^3\vec{r} \right|^2 \tag{2.26}$$

which means that the scattering intensity in reciprocal space represents the electron density of the material in real space.

2.3.2 Small Angle X-ray Scattering (SAXS)

Compared to the wavelength of X-rays, the size of nanoparticles is larger. Therefore, the larger the size ($d = \frac{2\pi}{q}$) to be detected, the smaller the scattering vector $\vec{q}$, which corresponds to a smaller scattering angle θ according to the equation 2.24. Thus, for the investigation of nanoscale structures, the angle between incident and scattered X-rays is very small ($0.1 \sim 10°$). This is the reason why SAXS is usually used to characterise nanoparticles.

For an ensemble of particles in SAXS, the scattering intensity is modified as follows:

$$I(\vec{q}) = \langle N \rangle F(\vec{q}) S(\vec{q}) \tag{2.27}$$

Where $\langle N \rangle$ is the average number of particles, $F(\vec{q})$ is the form factor, which represents the contribution of individual particles to the total intensity, while $S(\vec{q})$ is the structure factor, which describes the influence of interactions between particles on the intensity. Therefore, the scattered intensity curve in a monodisperse system appears like figure 2.7 (a).

The form factor is expressed as follows:

$$F(\vec{q}) = \left| \int_V \rho(\vec{q}) e^{-i\vec{q}\cdot\vec{r}} dV \right|^2 \tag{2.28}$$

Taking into account the polydispersity, i.e., the size of the particles are not uniform, the form factor can be written as follows

$$F(\vec{q}) = \frac{1}{N} \sum_i \left| \int_V \rho_i(\vec{q}) e^{-i\vec{q}\cdot\vec{r}} dV \right|^2 \tag{2.29}$$

The scattering intensity curve becomes a multi-peak in figure 2.7(b), and the form factor of a classical spherical particle can be simplified as follows:

$$F(\vec{q}) = \left| 3V_{sphere} \triangle\rho \frac{sin(\vec{q}R) - \vec{q}Rcos(\vec{q}R)}{(\vec{q}R)^3} \right|^2 \tag{2.30}$$

Where V is the volume of the particle, $\triangle\rho$ is the scattering length difference between the particle and the solvent, and R is the radius of the particle, while the structure factor can be described as follows:

$$S(\vec{q}) = 1 + 4\pi\rho \int [g(\vec{r}) - 1] \frac{sin\vec{q}R}{\vec{q}R} \vec{r}^2 d\vec{r} \tag{2.31}$$

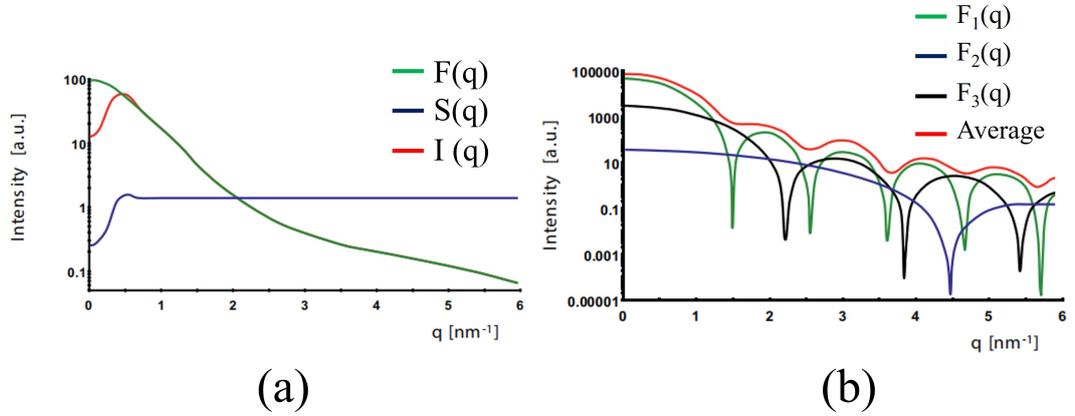Where $g(\vec{r})$ is the radial distribution function and ρ here is the particle density.

Figure 2.7: (a). Scattering intensity of particle dispersion (b). Form factor with different polydispersity [28]

2.3.3 Dynamic Light Scattering (DLS)

Visible light, in particular from laser sources, is also used to characterise particles. This technique can provide information on particles such as the hydrodynamic di-

ameter, diffusion coefficient, and molecular mass [29]. Depending on the detection methods and principles, light scattering is divided into static light scattering and dynamic light scattering. Figure 2.8 shows the schemes of these two measurements. Dynamic light scattering is more suitable for characterising the size distribution of nanoparticles in the solvent.
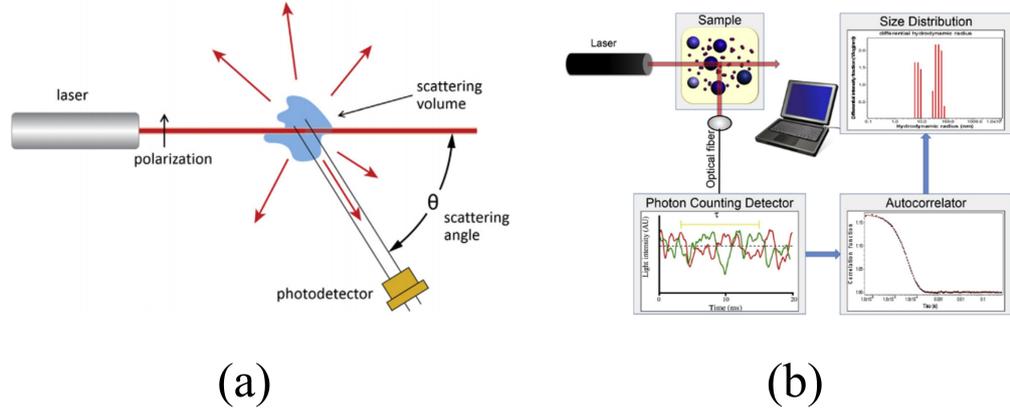

Figure 2.8: (a). Static light scattering (b). Dynamic light scattering

Dynamic light scattering is a type of time-resolved measurement that detects intensity fluctuations of scattered laser light with time due to thermal motion (Brownian motion) of particles in a solvent. The detected intensity fluctuates with time during the measurement. These fluctuations carry information about the diffusion behaviour of the particles, which is related to the particle size. The scattering vector q is expressed as follows:

$$q = \frac{4\pi n}{\lambda} sin(\frac{\theta_{DLS}}{2}) \tag{2.32}$$

Where n is the refractive index of the solution, λ is the wavelength of the laser, and θ_{dDLS} is the scattering angle.

The time variation of the scattered light intensity is characterised by the introduction of the autocorrelation function $C(q, \tau)$ as follows:

$$\frac{C(q,\tau)}{[I(q)]^2} = g^{(2)}(q,\tau) = 1 + \xi|g^{(1)}(q,\tau)|^2 \tag{2.33}$$

Where $I(q)$ is the average intensity ξ is an instrument coherence constant and $g^{(1)}$, $g^{(2)}$ are first and second order autocorrelation function respectively, $g^{(1)}$ is given as follows:

$$g^{(1)} = exp(-D_f q^2 \tau) \tag{2.34}$$

Where D_f is the diffusion coefficient obtained by fitting the experimental data. The hydrodynamic diameter of monodisperse particles can then be calculated according to the Stokes-Einstein relation, which is shown below:

$$d_h = \frac{k_B T}{3\pi\eta D_f} \tag{2.35}$$

Where d_h is the hydrodynamic diameter of the particle and η is the viscosity of the solvent. For particles with polydispersity, the hydrodynamic diameters could be calculated using the CONTIN (constrained regularisation for inverse problems) method [30].

It should be noted that the hydrodynamic diameter is larger than the physical core diameter of the particles because it includes not only the core diameter but also the ligand layer covering the particle surface, as shown in Figure 2.9. This difference could reach 40% or even higher [31].
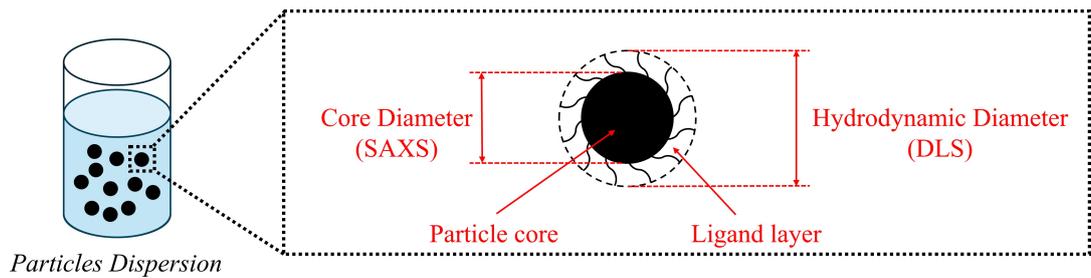

Figure 2.9: Core and hydrodynamic diameter

3 Experimental methods and Instruments

3.1 Materials

The nanoparticle dispersion used in this study is a commercial product (ID SOR-15-50) from Ocean Nano Tech, consisting of 15 nm iron oxide nanoparticles with a concentration of 25 mg/ml (T25 sample). These nanoparticles are coated with a hydrocarbon chain and dispersed in toluene. The nanoparticles consist of about 90% maghemite (γFe_2O_3) and 10% magnetite (Fe_3O_4) according to an earlier study [32]. In addition, toluene and polyethylene glycol (PEG 550) are used for dilution and viscosity adjustment. For our study, a certain amount of PEG 550 is added to 25 mg/ml nanoparticle dispersion to form 20 and 15 mg/ml nanoparticles dispersion with different viscosity (PT20 and PT15 samples) and another toluene diluted nanoparticle dispersions are prepared at the same concentrations (20 and 15 mg/ml) as references (T20 and T15 samples). PT20, and PT15 samples are prepared to study the influence of solvent viscosity on the structural properties. Only the magnetic properties of the T25 sample is studied and the 10 μg/ml nanoparticle in toluene dispersion (T$_{DLS}$ sample) was prepared for DLS measurements. Finally, six nanoparticle dispersions with different concentrations and different solvent viscosity are obtained as shown in the table 3.1.1.

Labels	Concentrations	Solvents	Measurements
T25(origin)	25 mg/ml	Toluene	Magnetometer, SAXS
T20	20 mg/ml	Toluene	SAXS
T15	15 mg/ml	Toluene	SAXS
PT20	20 mg/ml	20% PEG 550/Toluene 80%	SAXS
PT15	15 mg/ml	40% PEG 550/Toluene 60%	SAXS
T$_{DLS}$	10 $\mu g/ml$	Toluene	DLS

Table 3.1.1: Samples information on samples used in this study

3.2 Samples Preparation

Magnetic measurements

For magnetic characterisation, the sample has been placed in a specific position from one side of a plastic straw, 9 cm for MPMS and 12.5 cm for PPMS, as shown in figure 3.1 (a). A volume (10 μl) of nanoparticle dispersion is pipetted into the small plastic stamp, which is fixed twice in a cut pipette tip with a piece of sealing tape and covered with another piece of normal tape. Finally, the fixed stamp and straw are joined together, and any excess straw is cut off. It should be noted that the sample should stand up right throughout the process and should be handled carefully to prevent it from falling.

SAXS measurements

For the SAXS measurement, the nanoparticle dispersion is transported by a syringe into quartz capillaries, which are approximately 4 cm long for standard SAXS measurement and 1 cm long for field-assisted SAXS measurement, as shown in figure 3.1 (b), to different sample holders. In terms of dispersion volume, filling approximately half of the long capillary and a quarter of the short capillary gives the best results for standard and field applied SAXS measurements, respectively. The opening side of the capillary has been sealed with using a glue gun.

DLS measurments

For DLS measurement, the high-concentration nanoparticle dispersion has been first diluted to avoid complete laser absorption by a large number of particles. Therefore, 5 ml nanoparticle dispersion with a concentration of 10 μg/ml is prepared and then purified through a nano-sized filter to remove impurities. Finally, this dispersion is transferred by syringe into a pre-cleaned glass tube as shown in figure 3.1 (c).
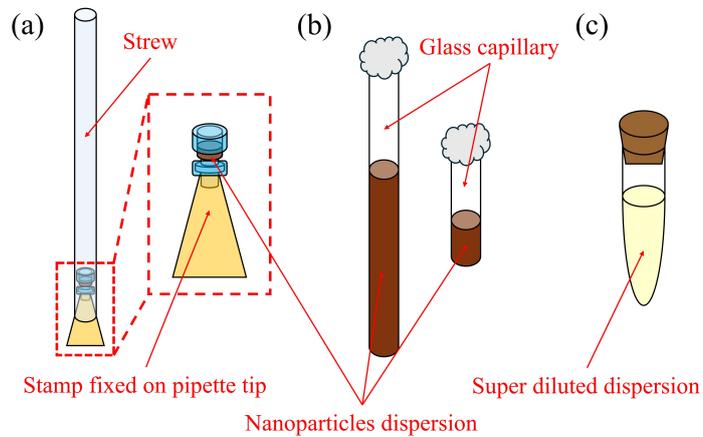
Figure 3.1: Schematic representation of sample preparation for (a) SQUID and PPMS, (b) SAXS and (c) DLS

3.3 Magnetic Characterizations

To investigate the magnetic properties of the nanoparticle dispersion, several measurements are performed, including hysteresis curve, zero field cooling/field cooling (ZFC/FC), AC susceptibility, magnetic relaxation, and memory effect analysis.

3.3.1 Instruments: MPMS-XL SQUID Magnetometer and PPMS System

In this study, the MPMS-XL SQUID magnetometer (figure 3.2 (a)) is used for hysteresis, zero-field cooling/field cooling, magnetic relaxation, and memory effect measurements, while the ACMS model of the PPMS (figure 3.2 (b)) is used for AC susceptibility measurements. Both instruments have a broad temperature range of 2 to 400 K, and the maximum magnetic field strengths are 7 T for the MPMS-XL SQUID magnetometer and $\pm$ 9 T for the ACMS model of the PPMS system. They are manufactured by the company Quantum Design and are located at the JCNS-2 Institute at the Jülich Research Centre, Germany.
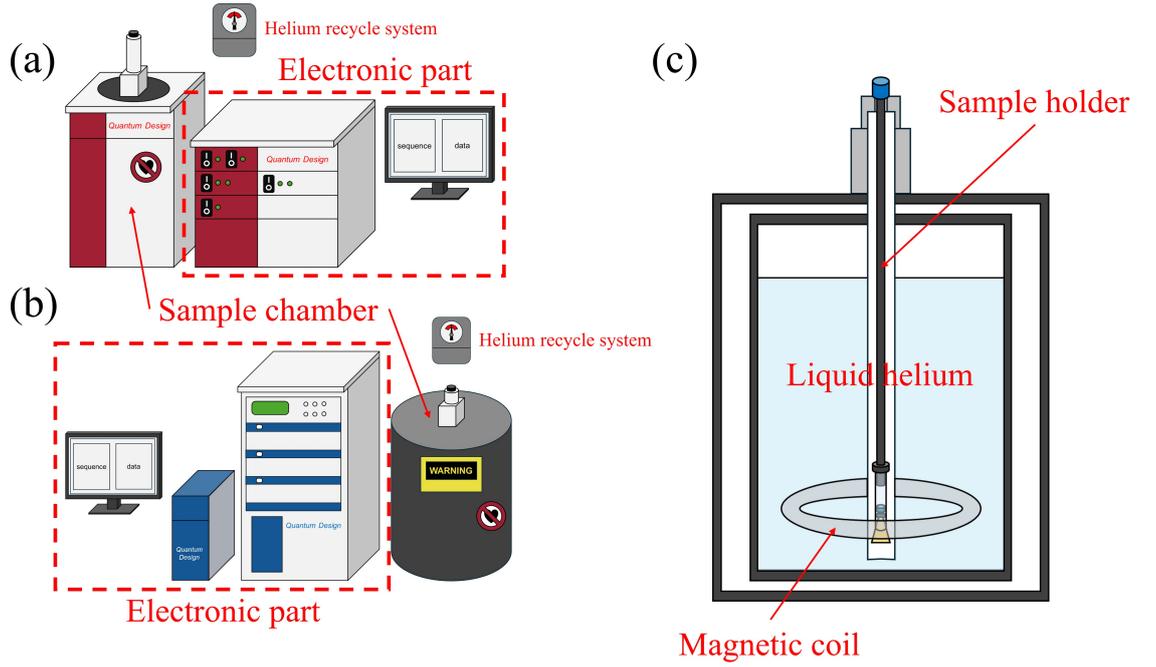
Figure 3.2: (a). MPMS-XL SQUID Magnetometer (b). PPMS system (c). Sample chamber

3.3.2 Hysteresis measurement: Magnetic field dependence

The hysteresis curve describes the magnetic response of materials to an external magnetic field (magnetic moment *vs*. field strength). For ferromagnetic or ferrimagnetic materials, the curve shows an open loop due to spontaneous alignment of magnetic moments, i.e., remanent magnetization, in materials without an external magnetic field. Several magnetic parameters can be obtained from the hysteresis curve, such as the saturation magnetization M_s, the remanent magnetization M_r, and the coercivity field H_c. The saturation magnetization M_s is the maximum magnetization when all magnetic moments are aligned with the applied field, while the remanent magnetization M_r is the magnetization without applied field, i.e., under zero field. The coercivity field H_c is the magnetic field strength used to reduce the magnetization of materials to zero. Depending on the strength of the coercivity field, materials can be classified as soft and hard magnetic materials, which show the ability to hold the magnetization. Figure 3.3 shows the hysteresis curves observed in different types of magnetic nanoparticles.
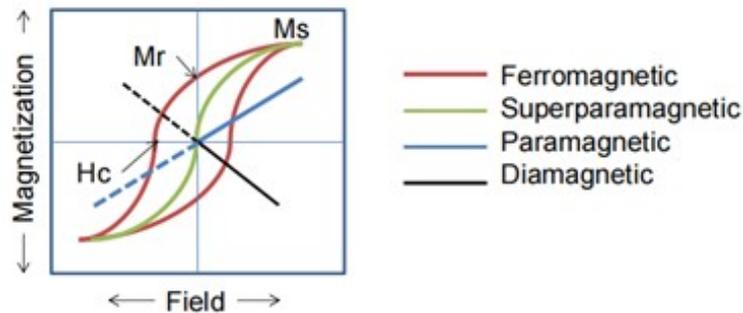
Figure 3.3: Hysteresis of different magnetic behaviors [33]

3.3.3 ZFC/FC: Temperature dependent magnetization

Zero field cooling and field cooling are two different ways of studying the magnetic behaviour of materials as a function of temperature (magnetic moment *vs*. temperature). The main difference between these two methods is that for ZFC the material is cooled without a magnetic field and the magnetic moments are measured during the heating process under an applied magnetic field, as shown in figure 3.4 (a), while for FC the magnetic moments of the material are measured during the cooling process with an applied magnetic field, as shown in figure 3.4 (b). The blocking temperature can be estimated from the temperature of the highest point in the ZFC curve after splitting the ZFC/FC curves (figure 3.5). The dispersion is cooled from 300 down to 10 K. The collective magnetic states of materials such as super spin glass (SSG) state or superferromagnetic (SFM) state can be distinguished by the memory effect, which is a characteristic feature of the SSG state. This effect is identified by comparing a reference ZFC magnetization curve with a memory effect ZFC curve in which the sample is held at a specific hold temperature for a prolonged period during the cooling process, as shown in figure 3.4 (c). If the material exhibits a SSG state at the holding temperature, there should be a peak in magnetization near this temperature [34]. In this study, the memory effect was measured at 80, 100, 120, 140, and 160 K.
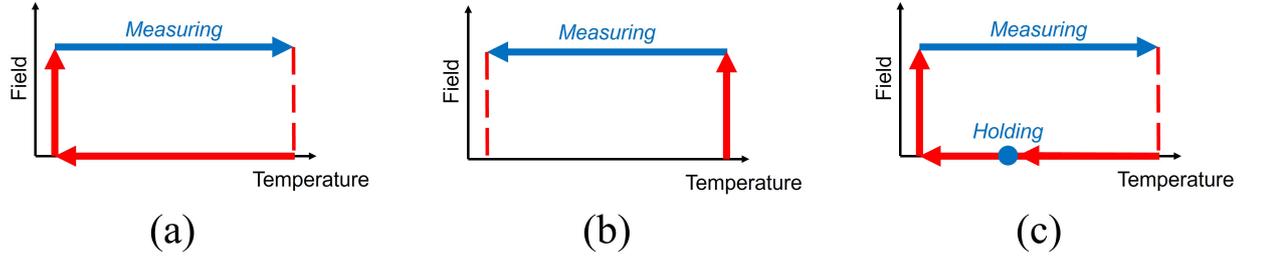
Figure 3.4: Illustration of the measurement of the (a). Zero field cooling (b). Field cooling and (c). Memory Effect
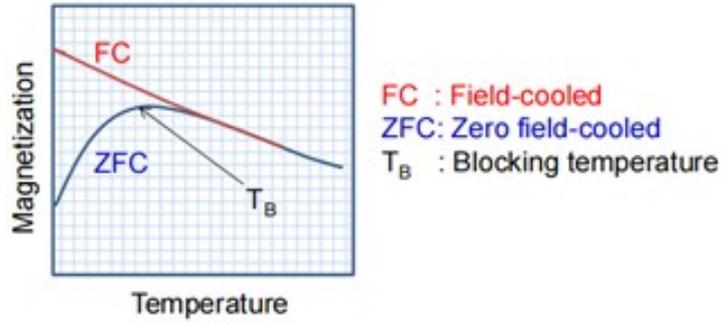

Figure 3.5: Blocking temperature T_b from ZFC/FC curves [33]

3.3.4 AC-Susceptibility: Frequency dependent magnetic response

AC susceptibility measurement uses an alternating magnetic field to express the magnetic behaviour of materials as a function of temperature at different frequencies. And susceptibility is described as follows [35]:

$$\chi = \chi' + i\chi'' \tag{3.1}$$

Where χ is the complex susceptibility, χ' and χ'' are the real and imaginary parts of the susceptibility, respectively. χ' represents the magnetic gain of materials, while χ'' represents the magnetic loss of materials. According to the Debye model, χ' and χ'' could be written as a function of frequency ($\omega = 2\pi f$):

$$\chi'(\omega) = \frac{\chi_0}{1 + (\omega\tau_{eff})^2} \tag{3.2}$$

$$\chi''(\omega) = \chi_0 \frac{\omega\tau_{eff}}{1 + (\omega\tau_{eff})^2} \tag{3.3}$$

$$\chi_0 = \frac{\mu_0 n m^2}{3k_B T} \tag{3.4}$$

Where χ_0 is the static susceptibility, ω is the frequency, τ_{eff} is the effective relaxation time, n is the particle density and m is the magnetic moment of a single particle. In this study, the measurements are carried out over the temperature range 10 to 300 K, field strength 0.8 mT, and frequencies 77, 177, 377, 777, 1777, 3777 and 7777 Hz.

3.3.5 Magnetic Relaxation: Time resolved magnetization

As introduced in section 2.2.5, magnetic relaxation refers to the time-dependent response of nanoparticles to changes in the magnetic field. This relaxation can occur via two mechanisms: rotation of the internal magnetic moment (Néel relaxation) or physical rotation of the entire nanoparticle (Brownian relaxation). In this study, the magnetic behaviour is measured by recording the magnetic moment as a function of time after the external magnetic field is switched off. To simplify the analysis, Brownian relaxation is neglected at temperatures below the melting point of the solvent (about 190 K for toluene) due to freezing of the medium. Therefore, only Néel relaxation is considered for the measured temperatures, i.e., 80, 100, 120, 140, 160, 180 K. Each relaxation measurement is carried out for 3000 s.
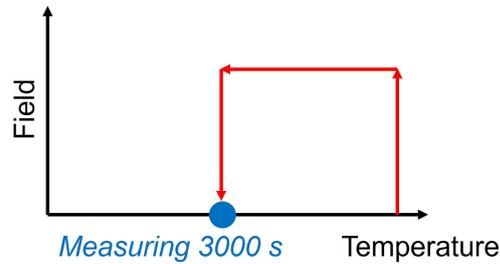

Figure 3.6: Illustration of the measurement of magnetic relaxation.

3.4 Structural Characterizations

To investigate the size, morphology, and field-dependent structural behaviour of the iron oxide nanoparticles, a combination of standard SAXS, field-assisted SAXS and DLS measurements were used.

3.4.1 Instruments

GANESHA: Standard SAXS and magnetic field-assisted SAXS measurements were performed using the GANESHA X-ray scattering instrument (Figure3.7(a)) at the JCNS-1 institute. X-rays with a wavelength of 0.13414 nm were generated by a Ga metal-jet source and detected by an EIGER 4M single-photon counting detector.

ALV/CGS-3 Platform: Dynamic light scattering (DLS) measurements were carried out using the ALV/CGS-3 Platform based Goniometer Systems at IBI-4 (Figure 3.7(b)). The setup uses a laser with a wavelength of 632 nm, and the detection angle between the incident laser and the detector is 90°.
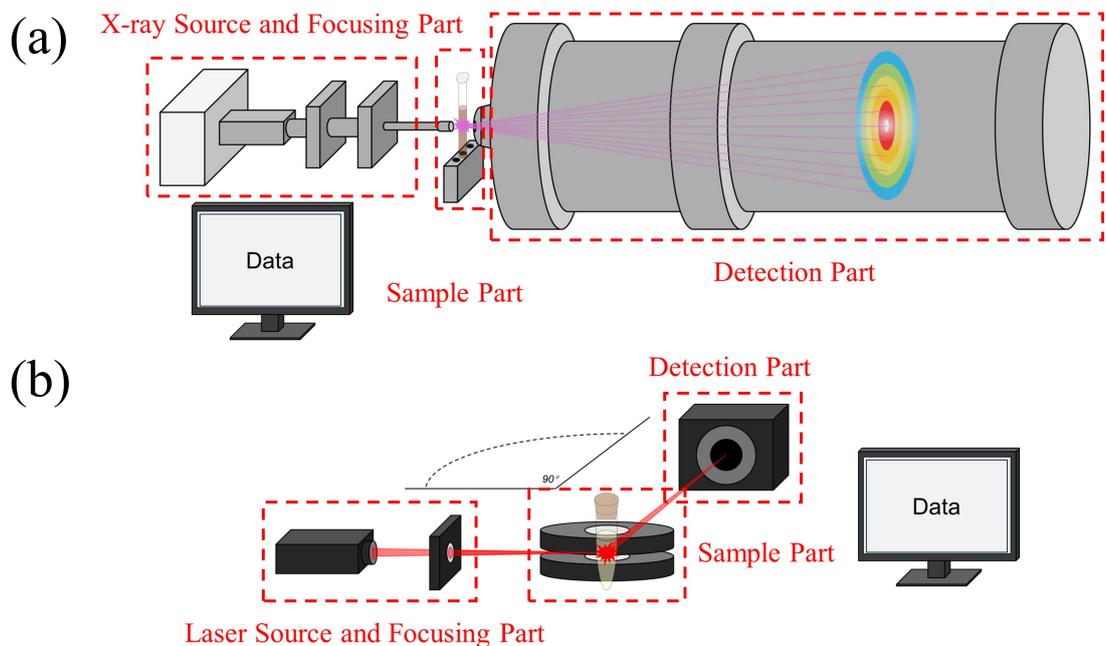

Figure 3.7: A schematic diagram of (a) Small Angle X-Ray Scattering and (b) Dynamic Light Scattering systems.

3.4.2 Standard Small Angle X-ray Scattering

The basic principles of SAXS have already been introduced in sections 2.3.1 and 2.3.2 The standard SAXS measurements in this study were performed at room temperature, with each sample measured for 5 minutes. The resulting data were reduced using a Python script and then fitted using SasView 6.0.1 software [36], applying various models such as the spherical form factor, hard sphere and sticky hard sphere models. From these fits, the core diameter and size distribution of the nanoparticles were determined. Depending on the model chosen, additional parameters such as volume fraction, stickiness and interparticle interaction strength were also obtained. Five nanoparticle samples, T25, T20, T15, PT20, and PT15, were investigated. By comparing the SAXS results across these samples, the effects of particle concentration (T25, T20, and T15) and solvent viscosity (T20 vs. PT20 and T15 vs. PT15) on particle size and inter-particle interactions were analysed. For accurate background subtraction, measurements of the pure solvents corresponding to each sample were also carried out.

3.4.3 Small Angle X-ray Scattering under Magnetic field

In contrast to standard SAXS, these measurements were carried out under an applied external magnetic field, generated by two magnets integrated into a mechanical sample holder, as shown in figure 3.8. The magnetic field is oriented vertically. Each measurement lasts 300 s, during which the magnetic field is applied for the first 60s and then turned off. A key distinction in this experiment is the analysis of the azimuthal distribution of the scattering intensity, which provides direct insight into the structural orientation of the nanoparticles and the effect of the magnetic field on their arrangement. The same five samples—T25, T20, T15, PT20, and PT15—were examined, enabling investigation of the influence of particle concentration and solvent viscosity under the influence of an external field.
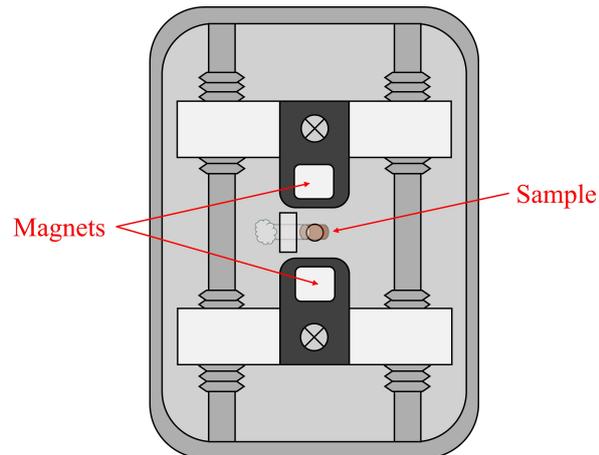
Figure 3.8: Mechanical sample holder equipped with two magnets for applying an external magnetic field during SAXS measurements.

3.4.4 Dynamic light scattering

The principle of DLS has already been introduced in section 2.3.3. Each measurement in this study was performed at room temperature for a duration of 300s, with data analysis performed automatically by the instrument software. The resulting outputs include the correlation function, the count rate and the calculated hydrodynamic diameter distribution.

Due to concentration limitations, all DLS measurements were performed at a fixed nanoparticle concentration of 10 μg/ml. The T$_{DLS}$ sample was thus prepared and analysed.

4 Results and Discussion

4.1 Magnetic Properties

4.1.1 Hysteresis Loop

Figure 4.1 shows the hysteresis loops of the T25 sample measured at different temperatures. A clear open loop is observed at 10 K (black curve in figure 4.1(a)), indicating significant remanent magnetization and coercivity. At higher temperatures, the loops exhibit a typical S-shape with negligible coercivity and remanent magnetization, reflecting unblocked superparamagnetic behaviour as shown in figure 4.1(a). According to the equation 2.20, the Néel relaxation time of nanoparticles or superspins increases with decreasing temperature. Once the relaxation time exceeds the time window of a recorded point, the magnetization of nanoparticles can be measured as a non-zero value even without a magnetic field, while a collective state, such as the superspin glass state or the superferromagnetic state, also leads to remanence. Thus, one cannot simply decide whether this remanence is induced by collective ordering or very slow relaxation. As the temperature increases, the nanoparticles or superspins have more thermal energy to overcome the magnetic anisotropy barrier, then the superspins can align freely and more easily with the magnetic field. Therefore, the coercivity and remanence in the loop become smaller (figure 4.1(b)), and the S-shape is observed.

In addition, at 10 K, a small shift observed in the hysteresis loop could result from the exchange bias effect. This phenomenon is an interfacial exchange interaction between ferromagnetism and antiferromagnetism, or ferromagnetism and ferrimagnetism [37]. Due to the different arrangement of magnetic moments at the ferromagnetism/antiferromagnetism (ferrimagnetism) interface, the interfacial exchange
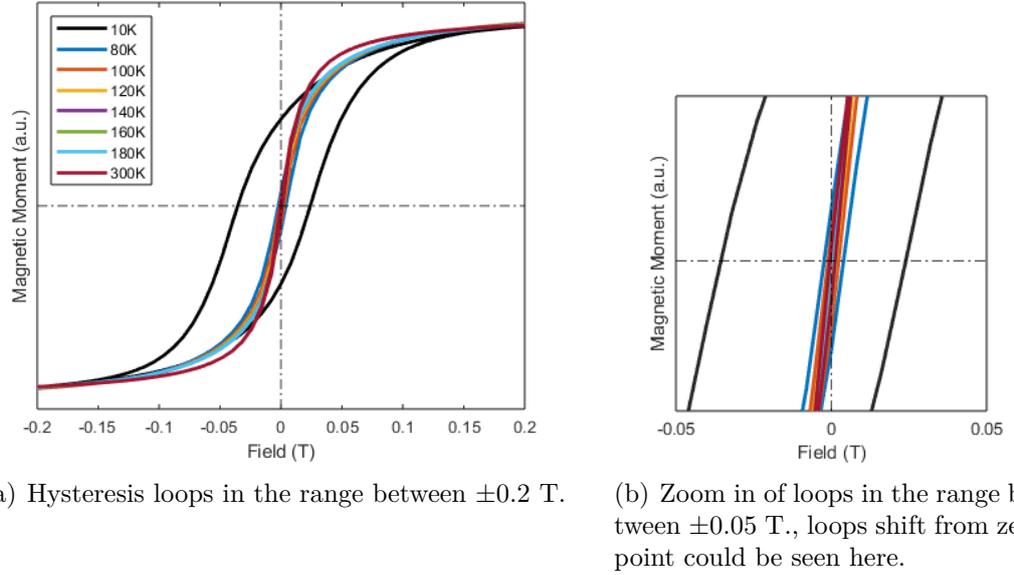
(a) Hysteresis loops in the range between ±0.2 T.

(b) Zoom in of loops in the range between ±0.05 T., loops shift from zero point could be seen here.

Figure 4.1: Hysteresis loop of T25 sample at 10, 80, 100, 120, 140, 160, 180 and 300 K.

interactions can hinder the ferromagnetic moments to align with the field in some direction, and this hindering is shown as the bias of the loop from the centre point.

4.1.2 Zero Field Cooling and Field Cooling

Figure 4.2(a) shows the magnetic behaviour of the T25 sample under zero field cooling (ZFC) and field cooling (FC). In the ZFC curve (red line in figure 4.2(a)), the magnetisation increases with temperature up to about 216 K. Beyond this temperature, the magnetization decreases up to 288 K, where it suddenly increases, followed by a gradual decrease up to 300 K. This behaviour is strongly dominated by the thermal energy [38] and can be attributed to the thermal activation of magnetic relaxation and thermal fluctuations.

When a small magnetic field is applied, the magnetic anisotropy energy dominates the rotation of the magnetic moments according to the equation 2.12. At low temperatures, nanoparticles do not have enough thermal energy $E_{thermal} = k_B T$ to overcome the magnetic anisotropy energy barrier of magnetic anisotropy E_K. Thus, most nanoparticles or superspins are confined along their easy magnetic axis. Since the orientation of the easy axis of each superspin is random, very little magnetiza-
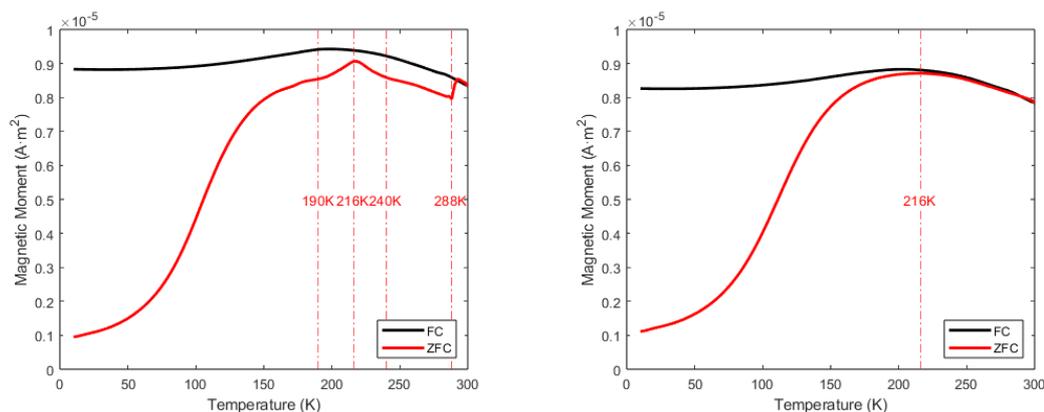
(a) ZFC/FC curve of T25 sample, kinks of ZFC curve at 190, 216, 240 and 288 K.

(b) Dried T25 sample, peak of ZFC curve at 216 K

Figure 4.2: ZFC/FC curves of T25 sample and dried T25 sample

tion is observed at low temperatures.

When temperature increases, more nanoparticles are thermally activated, thus, their superspins can align with the external field through Néel relaxation. This leads to an increase in the magnetization and forms the smooth peak around 150 K. Once the temperature reaches the melting point of toluene (around 190 K), Brownian relaxation is available, allowing further alignment of the superspins with the applied field through mechanical rotation of nanoparticles. This process appears as the first kink in figure 4.2(a), indicating a combination of both Néel and Brownian relaxation. As the temperature is further increased, the influence of thermal fluctuation becomes apparent, especially around 216 K, where a drop in magnetization is observed. This suggests that the toluene is gradually melting due to an unknown effect over a wide temperature range. If so, the second bend at 240 K could be a sign of complete melting of the toluene. The sharp peak at 288 K suggests that toluene absorbs a small amount of water from the ambient air. This may enhance the Brownian relaxation and contribute to further alignment of the superspins. When compared to the ZFC curve of the dried T25 sample (red line in figure 4.2(b)), no such sharp peaks are observed and the highest value of the magnetization is still clearly around 216 K. Therefore, solvent melting is likely to be the reason why two additional sharp peaks appear in the ZFC curve of the fresh T25 sample, and why thermal fluctuations become more significant above 216 K.

The FC curves of the T25 sample and the dried T25 sample (black lines in figures 4.2(a) and 4.2(b)) have a wave-like shape, probably because the thermal fluctuations
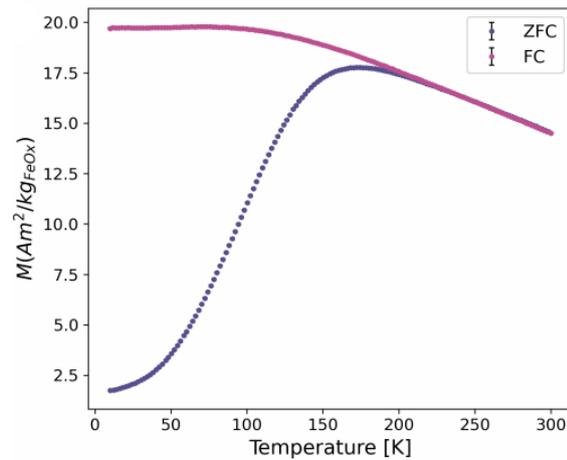
Figure 4.3: ZFC/FC curves of 15 nm superparamagnetic iron oxide nanoparticles in toluene [39], peak of ZFC curve at 172 K, corresponding to the block temperature.

decrease with temperature. After cooling below 216 K, the magnetization decreases slightly, implying that this system is gradually transitioning to a more stable magnetic state. However, a previous study [39] reported a blocking temperature of 172 K for 15 nm superparamagnetic iron oxide nanoparticles in toluene (Figure 4.3), which is significantly lower than the 216 K observed here. This contradiction suggests that there may be strong interparticle magnetic interactions between nanoparticles in the T25 sample.

Figure 4.4 shows the ZFC behaviour of the T25 sample under different magnetic field strengths. As the magnetic field strength increases, the smooth peak of the ZFC curves (blue, orange and yellow lines in Figure 4.4) shifts to lower temperature and higher magnetization. This means that a stronger magnetic field helps superspins to overcome the magnetic anisotropy barrier with less thermal activation. When the magnetic field is larger than 100 mT, the superspins can align directly with the field, so that the ZFC curves (violet and green lines in the figure 4.4) are almost flat from 10 to 300 K. In addition, the sharp peak in the ZFC curves appears at higher temperatures and becomes flatter when comparing 5, 20 and 100 mT, which could be a result of the temperature-induced toluene volatilisation. One can see the difference in volume of dispersion before (Figure 4.4(b) left) and after (Figure 4.4(b) right) measurements, which supports this interpretation.
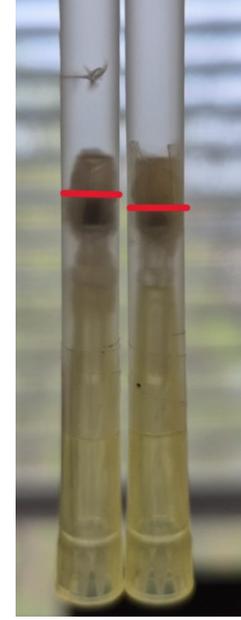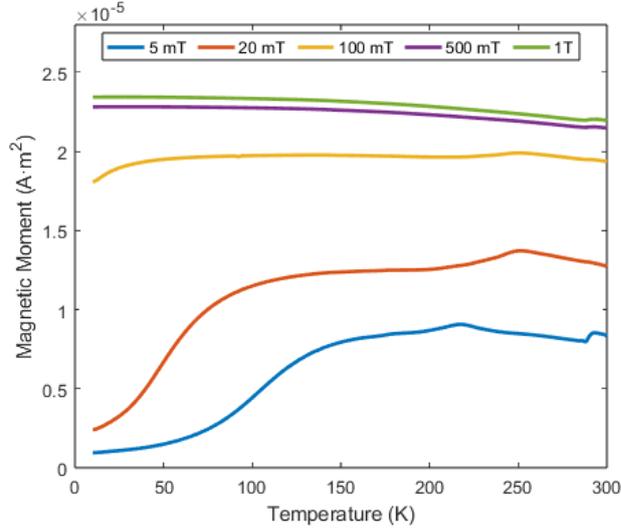
(a) ZFC curves of T25 sample under 5, 20, 100, 500 mT and 1 T.

(b) T25 samples, right: before measurement, right: after measurement (red line represents liquid level).

Figure 4.4: ZFC curves of T25 sample as a function of magnetic field.

4.1.3 AC-Susceptibility

Figure 4.5 shows the AC susceptibility of the T25 sample measured at different frequencies. The real part of the susceptibility (figure 4.5(a)) shows a clear increase between 80 and 250 K, which means that the system starts to effectively gain energy from the applied AC magnetic field through magnetic relaxation (Néel and Brownian relaxation). After reaching a peak, all curves fall along the same line, which could be due to the thermal fluctuations that dominate at higher temperatures. In the imaginary part of the susceptibility (Figure 4.5(b)), all curves have a symmetrical shape with a single peak, and this peak corresponds to the highest dissipation. According to equation 3.3, the imaginary part of the susceptibility is maximal when $\omega\tau_{eff} = 1$ is satisfied, while equation 2.22 shows that there is a negative correlation between the effective relaxation time and the temperature. Thus, once the effective relaxation time reaches the value that can satisfy the condition $\omega\tau_{eff} = 1$, the
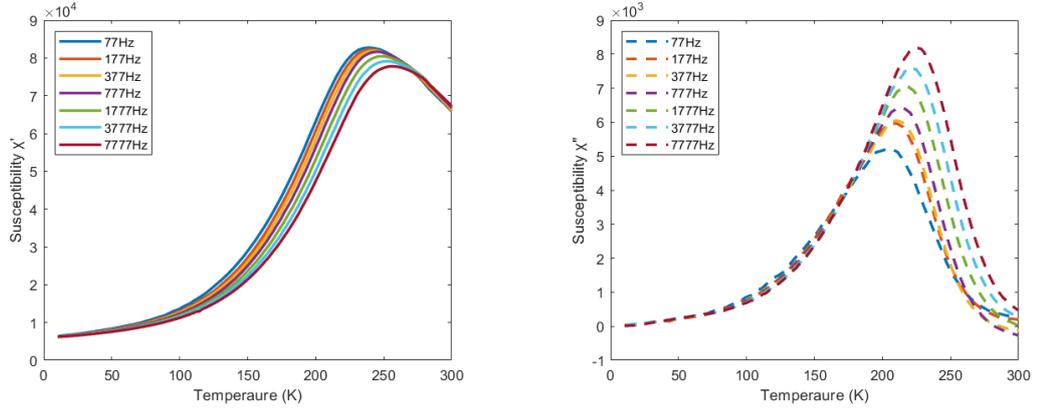
(a) Real part of the susceptibility χ', reflecting energy gain from alternative magnetic field.

(b) Imaginary part of the susceptibility χ'', reflecting energy dissipation in alternative magnetic field.

Figure 4.5: AC-susceptibility of T25 sample with 77, 177, 377, 777, 1777, 3777 and 7777 Hz.

system has maximum energy dissipation that is transferred to heat, and this is the principle of magnetic hypothermia. This energy dissipation, especially in the high-frequency range, directly relates to the heating efficiency in magnetic hyperthermia applications. Therefore, analyzing AC susceptibility provides critical insight into optimizing nanoparticle formulations for therapeutic heat generation.

Figure 4.6 plots the peak temperatures of the imaginary susceptibility *vs.* the corresponding matched frequencies, and Table 4.1.2 presents the fitting results obtained using the equations 2.15 and 2.18 used to distinguish the magnetic state of T25 sample. Both models show a good fit (see the R^2 value in the table 4.1.2). However, the fitted trial time (here $\tau_0 = 1.3 * 10^{-24}$ s) of the superparamagnetism (SPM) model is totally beyond $10^{-9} \sim 10^{-12}$ s, which is insignificant and physically meaningless. The fitting parameters from the superspin glass state (SSG) or superferromagnetism (SFM) model are more reasonable. The experimental time is $4.2 * 10^{-9}$ s, the transition temperature is 160 K, and the critical exponent is $zv = 10.02$. These results confirm that the T25 sample transits to a collective magnetic state (SSG or SFM) below a critical temperature around 160 K.
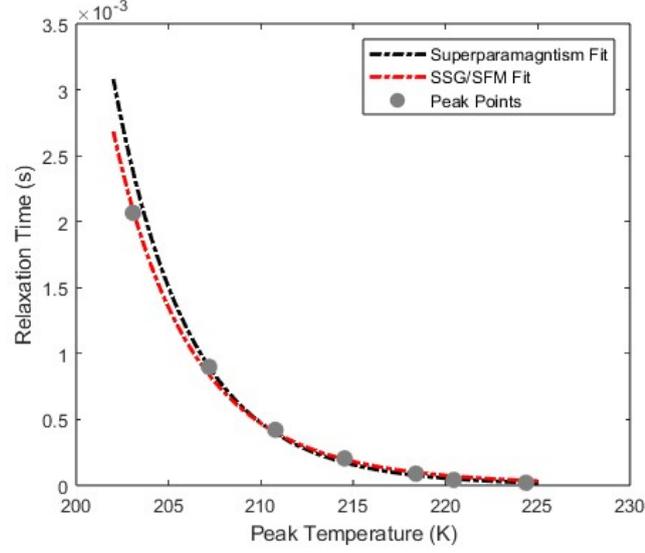
Figure 4.6: Relationship between temperature and relaxation time, fitted by SPM (equation 2.15) and SSG/SFM (equation 2.18).

Temperature (K)	$\tau=\frac{1}{2\pi\omega}$ (s)
203.07	$2.10 * 10^{-3}$
207.19	$8.99 * 10^{-4}$
210.78	$4.22 * 10^{-4}$
214.53	$2.05 * 10^{-4}$
218.39	$8.96 * 10^{-5}$
220.45	$4.21 * 10^{-5}$
224.36	$2.05 * 10^{-5}$

Table 4.1.1: Peak temperatures of imaginary susceptibility χ'' and corresponded relaxation time τ.

SPM fit results	SSG/SFM fit results
$\tau = \tau_0 exp(\triangle E^*/k_b T)$	$\tau = \tau_0(\frac{T-T_{c,g}}{T_{c,g}})^{-zv}$
$\tau_0 = 1.3 * 10^{-24}$ s	$\tau_0 = 4.2 * 10^{-9}$ s
$\triangle E^*/k_b T = 9942.1$	$-zv = -10.02$
	$T_{c,g} = 160$ K
$R^2 = 0.993$	$R^2 = 0.998$

Table 4.1.2: Fit result of SPM and SSG/SFM, τ is the relaxation time, τ_0 is the attempt time and $T_{c,g}$ is the critical temperature, R^2 represents fit quality.

4.1.4 Magnetic Relaxation

Figure 4.7 shows the magnetic relaxation behaviour and its corresponding relaxation rate over a period of 3000 s of the T25 sample at different temperatures. The magnetic relaxation rate $W(t) = -\mathrm{d}ln[m(t)]/\mathrm{d}t = At^{-n}(n > 0)$ is a universal expression to describe the relaxation behaviour of an ensemble of superspins with random spatial distribution, anisotropy and spin sizes [40]. The value of n reflects the degree of interaction within the system. Further studies have induced three different decay troughs of the magnetic moment $m(t)$, depending on the value of n, as follows [41]:

$$Exponential\ decay: m(t) \simeq m_0\ exp[-(\frac{t}{\tau})^{1-n}]\ (0 \leq n < 1) \qquad (4.1)$$

$$Power\ law\ decay: m(t) \simeq m_1\ t^{-A}\ (n = 1) \qquad (4.2)$$

$$Power\ law\ decay\ with\ remanence: m(t) \simeq m_\infty + m_1\ t^{1-n}\ (n > 1) \qquad (4.3)$$

Where m_0, m_1, m_∞ and τ are fitting parameters. Therefore, $0 < n < 1$ corresponds to a system with weak interaction, while $n > 1$ corresponds to a system with strong interaction, and $n = 1$ represents a critical value to separate weak and strong interaction. In several studies of magnetic thin films [34, 41], $n > 1$ and $n < 1$ are associated with super spin glass (SSG) and superferromagnetic (SFM) behaviour, respectively. These interpretations may apply to the nanoparticle dispersion system studied in this project.
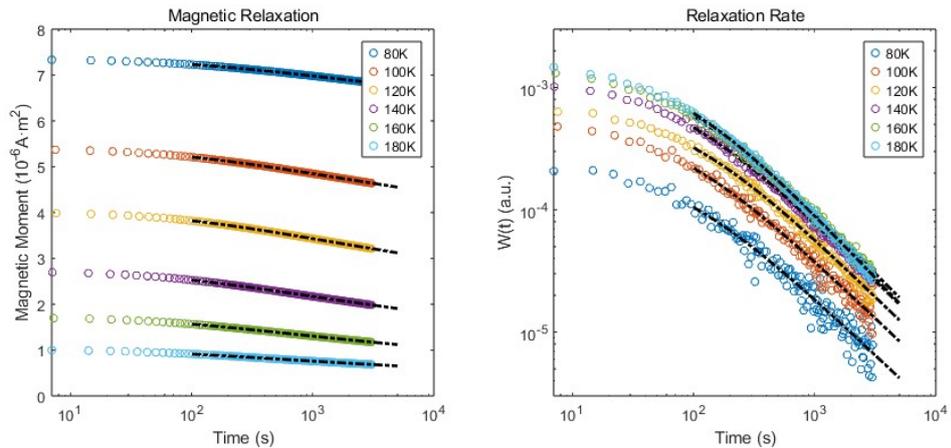

Figure 4.7: Magnetic relaxation and relaxation rates of T25 sample at 80, 100, 120, 140, 160 and 180 K.

Table 4.1.3 shows the best results of n values obtained by fitting the relaxation data $m(t)$ with the equations 4.1, 4.2 and 4.3. It also includes the calculated $n*$ values driven by the relaxation rate $W(t)$, a long with the relaxation amount $\triangle m$ over 3000s. The values of n and n^* increase with temperature and both cross the line of $n = 1$, which means that this system has non-negligible interparticle interactions and is probably close to the transition regime between SSG and SFM states at the investigated temperatures.

Temperature (K)	n	n* ($W(t)$)	$\triangle$m
80	0.98 (Eq.4.1)	0.95	7.01%
100	1.00 (Eq.4.2)	0.96	13.92%
120	1.00 (Eq.4.2)	0.97	19.83%
140	1.08 (Eq.4.3)	0.98	27.00%
160	1.12 (Eq.4.3)	1.00	31.44%
180	1.18 (Eq.4.3)	1.05	31.83%

Table 4.1.3: Values of n, n* and relaxation amount $\triangle$m of T25 sample.

This transition could be explained as follows: At low temperature, the system will behave as SSG, where all the superspins are frozen in a metastable configuration, as shown in figure 4.8 (left), due to the magnetic frustration coming from the competition of nanoparticle interactions (parallel vs. antiparallel). All of these sub-stable states are equally energetically and magnetically disordered. Increasing the temperature leads to more thermal energy, and this will disrupt the magnetic frustration. Hence, the uniform alignment of the superspins becomes more favourable. This leads to a transition to the SFM state with magnetic domains (figure 4.8 (right)).

Sub-stable States of SSG   *SFM*
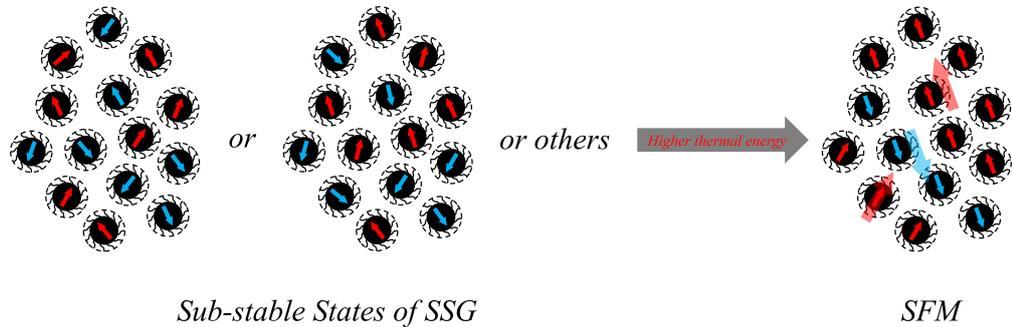
Figure 4.8: Evolution of magnetic states in nanoparticles with changing temperature: Transition from a spin-glass-like to an ordered superparamagnetic state as temperature increases.

4.1.5 Memory Effect

Figure 4.9 shows the memory effect measurements of T25 at different temperatures. The ZFC curves are shown in Figure 4.9(a), and the subtraction of the ZFC curves $(m_T - m_{ref.})$ is plotted in Figure 4.9(b) to identify whether or not the memory effect is present in the T25 sample. These data, which represent clear peaks, appear around each hold temperature in Figure 4.9(b), indicating that memory effects are indeed present. In addition, the deviation from the reference ZFC curve decreases with increasing temperature. This result is consistent with the critical or glass temperature of 160 K determined in section 4.1.3, suggesting that the T25 sample behaves as a superparamagnet above 160 K. Thus, the memory effect is demonstrated at any holding temperature, which means that T25 is more likely to be in a superparamagnetic glassy state below 160 K.
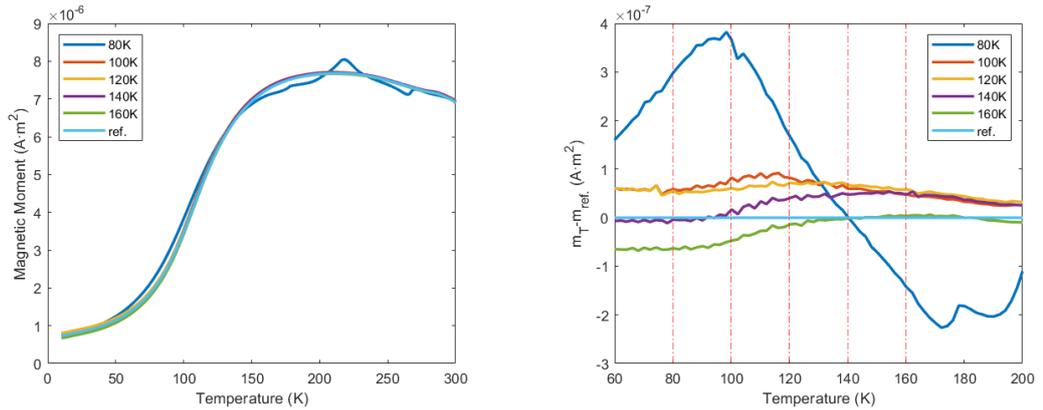
(a) ZFC curves of T25 sample at waiting temperatures for 3600 s.

(b) Bias from reference of memory effect measurement ZFC curves

Figure 4.9: Memory effect of T25 sample at 80, 100, 120, 140, 160 and 180 K.

4.1.6 Summary

In this section, the magnetic properties of the T25 sample, such as hysteresis behaviour, temperature dependence of magnetic moment, AC-susceptibility, and relaxation rate, have been studied at different temperatures. At low temperature (10 K), due to the lack of thermal activation, this system is 'frozen' in a quasi-static state. In this state, although the superspins tend to align with the external magnetic field,

the relaxation process is super slow (on the order of years or longer) and could be considered 'blocked'. However, when no magnetic field is applied, the superspins are locked in the direction of the magnetic easy axis. With increasing temperature, magnetic relaxation is activated by thermal activation, i.e., the thermal energy of the superspins is high enough to overcome the energy barrier of magnetic anisotropy and more and more superspins start to align with the field until the influence of thermal fluctuations becomes noticeable, which can then break the alignment of the superspins. According to the interaction strength of the T25 sample, shown as the red line in figure 4.10, the T25 sample exhibits a collective magnetic state known as the supoerspin glass state (SSG) below the glass temperature of 160 K. Above this temperature, the T25 sample changes to the superparamagnetic state (SPM).
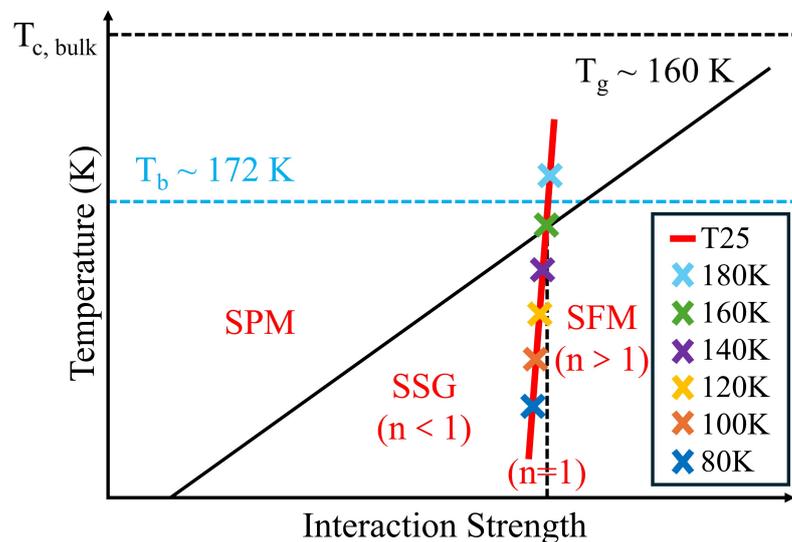

Figure 4.10: Magnetic phase diagram of T25 sample, red line represents the interaction of T25 sample.

4.2 Structural Properties

4.2.1 Standard SAXS

Nanoparticles in pure Toluene

Figure 4.11 shows the standard SAXS results for the T25 sample. In figure 4.11(a), the data of the T25 sample have been fitted assuming a spherical form factor without including the structure factor. Additionally, the low Q region was analysed using the Guinier function [42] as shown in the inset of figure 4.11(a). However, both fits show deviations, which means that the T25 sample has interparticle interaction even at a very low concentration (25 mg/ml). Therefore, the structure factor must be considered for further analysis. The fitted radius of the spherical particles, R_0, is 7.1(1) nm, while the radius of gyration from the Guinier fit is 6.6(1) nm, which corresponds to a spherical radius of 8.5(2) nm. This slightly larger radius value is due to a small deviation from the linear behaviour of ln(intensity) vs Q^2 in the low Q region, this deviation has also been observed in the form of non-linear curvature in the Guinier plot at $Q^2 < 0.03$ nm^{-2}, which corresponds to 18 nm and larger radius, indicating slight nanoparticle aggregation.

(a) Sphere and Guinier fit of T25 sample.   (b) Hardsphere and Stickyhardsphere fit of T25 sample.
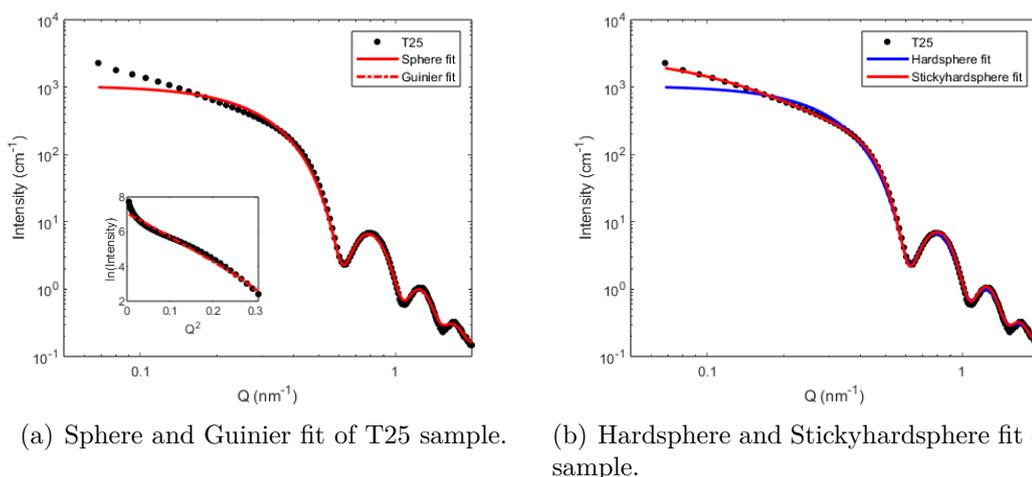
Figure 4.11: SAXS data of T25 sample, fitted by sphere, hardsphere (HS) and stickyhardsphere (SHS) model, and Guinier model in low Q range.

Samples	$R_0(nm)$	σ (polydispersity)	$R_g[R_c]$(nm)	R_{eff}(nm)	Vol.	ϵ	τ
T25	7.1(1)	7.5(6)%	6.6(0) [8.5(2)]	7.1(5)	2.4(9)%	0.081(5)	0.1
T20	7.1(1)	7.1(8)%	6.6(7) [8.6(1)]	7.1(5)	1.7(9)%	0.069(7)	0.1
T15	7.1(7)	7.0(4)%	6.6(9) [8.6(4)]	7.1(5)	1.4(6)%	0.063(9)	0.1

Table 4.2.1: Fitting parameters for T25, T20 and T15 samples, R_0 is the spherical radius, σ is the log-normal standard deviation, $R_g[R_c]$ are the gyration radius and correspond spherical radius, R_{eff} is the effective radius of stickyhard sphere, Vol. is the volume fraction, ϵ is the stickiness and τ is the perturbation.

To determine the nature of the interparticle interactions in the T25 sample, the data were also fitted using a sphere model with structure factors: the Hard Sphere (HS) model and the Sticky Hard Sphere (SHS) model. Figure 4.11(b) clearly shows that the SHS model provides a significantly better fit than the HS model. Therefore, the nanoparticles in the T25 sample have not only exclusion interactions but also short-range attractive interactions between them, probably due to van der Waals forces between surface atoms (Fe and O) of nanoparticles and solvent molecules (toluene), or other interparticle forces. The same behaviour is observed for the T20 (20 mg/ml) and T15 (15 mg/ml) samples in figure 4.12. The SHS model fits them very well, and the resulting fitted parameters of T25, T20 and T15 samples are very close to each other (see table 4.2.1), especially the radius. Thus, within this dilution range, the interparticle interaction between nanoparticles dispersed in toluene remains largely unchanged. Slight aggregation and attractive short-range interparticle interactions are present in all three samples (T25, T20 and T15).

Nanoparticles in PEG550/Toluene mixture

Figure 4.13 shows the standard SAXS results of PT20 and PT15 samples, and the corresponding fitting parameters are summarised in Table 4.2.2. The particle size and size distribution of the PT20 sample are similar to those obtained for the T25, T20 and T15 samples. The SHS model gives a good fit for PT20 as shown in Figures 4.13(c), while PT15 deviates significantly from the spherical model in the low Q region as shown in Figure 4.13(b). In addition, a distinct peak appears around 0.4 nm^{-1}. These results indicate that the addition of polyethylene glycol 550

(a) Sphere and Guinier fit of T20 sample.

(b) Sphere and Guinier fit of T15 sample.

(c) Stickyhardsphere fit of T20 sample.

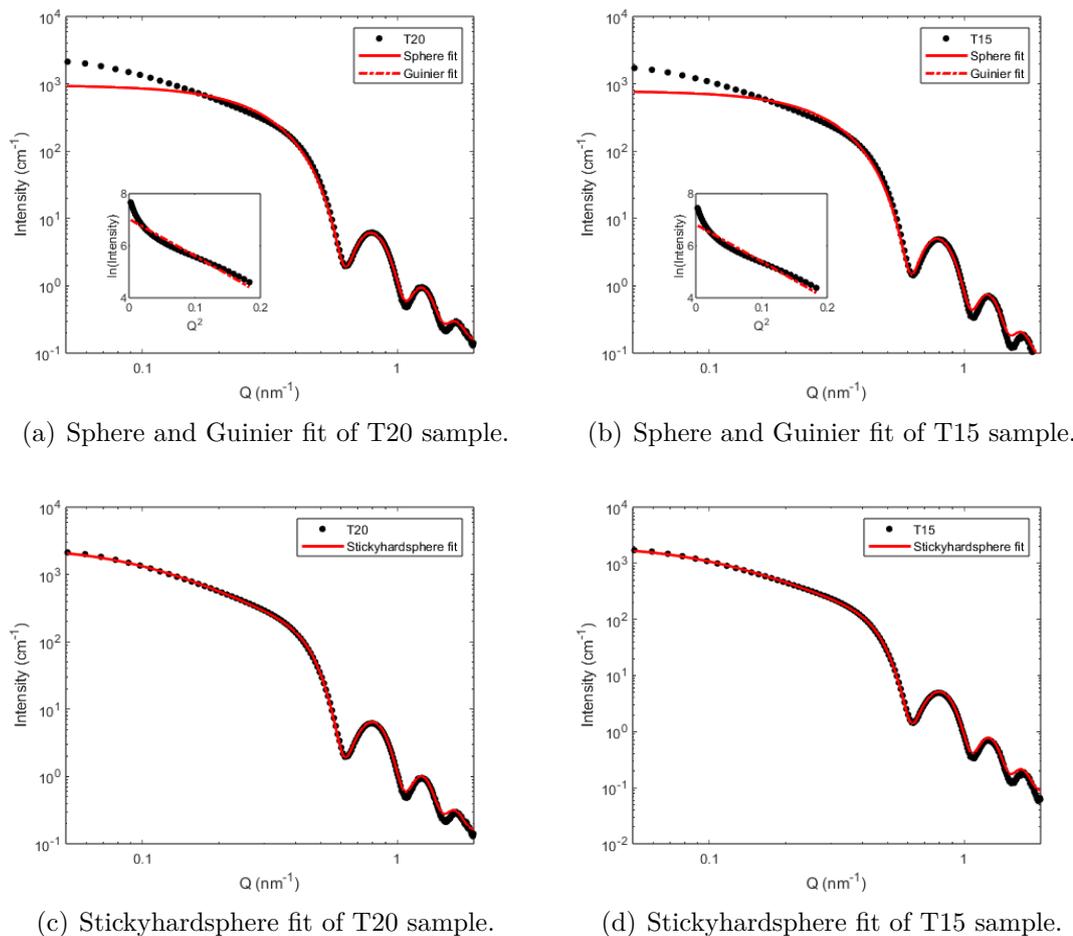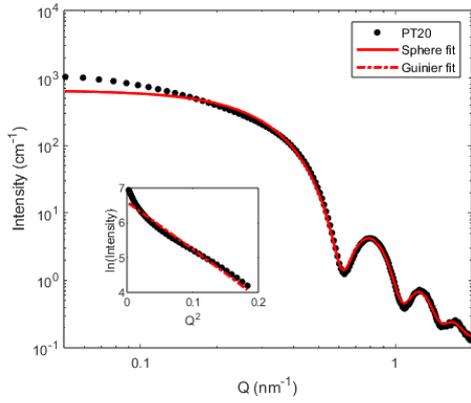(d) Stickyhardsphere fit of T15 sample.

Figure 4.12: SAXS data of T20 and T15 samples, fitted by sphere and stickyhard-sphere (SHS) model, and Guinier model in low Q range.

(PEG 550) affects the interparticle interactions. Adding 20% PEG 550 (PT20) into toluene does not significantly affect the interparticle interactions in PT20. However, when the amount of PEG 550 is increased to 40% (PT15), the nanoparticles aggregate strongly, probably due to changes in the solvent environment, which can be attributed to the limited miscibility and strong polarity contrast between PEG 550 and toluene. This likely leads to microphase separation or PEG 550-rich domains within the solvent, creating a heterogeneous environment that destabilizes the nanoparticle dispersion. Additionally, PEG 550 molecules may bridge between nanoparticle surfaces or alter the local solvation shell, promoting attractive interactions and resulting in rapid aggregation. The corresponding core radius R_c and effective radius R_{eff} of PT15 sample, which are very large compared to the rest samples, support the occurrence of aggregation.

| Samples	$R_0(nm)$	σ (polydispersity)	$R_g[R_c]$(nm)	R_{eff}(nm)	Vol.	ϵ	τ
PT20	7.1(2)	7.3(6)%	6.6(1) [8.5(3)]	7.1(2)	1.2(6)%	0.066(3)	0.1
PT15	7.4(1)	7.1(8)%	28.0(5) [36.2(1)]	7.4(2)	31.8(4)%	0.007(1)	0.1

Table 4.2.2: Fitting parameters for PT20 and PT15 samples, R_0 is the spherical radius, σ is the log-normal standard deviation, $R_g[R_c]$ are the gyration radius and correspond spherical radius, R_{eff} is the effective radius of stickyhard sphere, Vol. is the volume fraction, ϵ is the stickiness and τ is the perturbation.
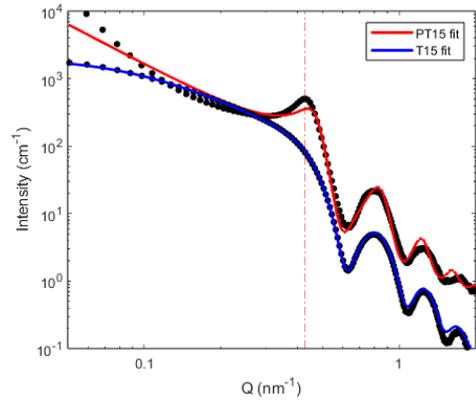

(a) Sphere and Guinier fit of PT20 sample.
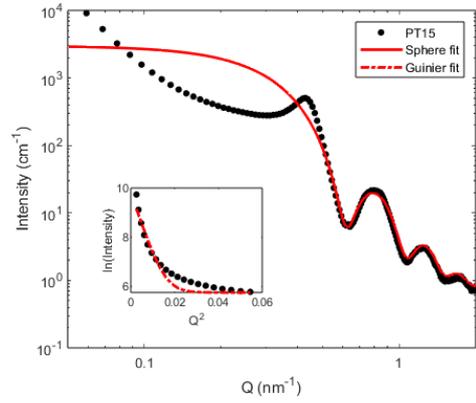
(b) Sphere and Guinier fit of PT15 sample.
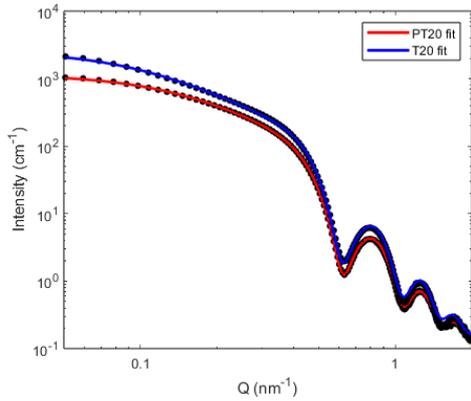
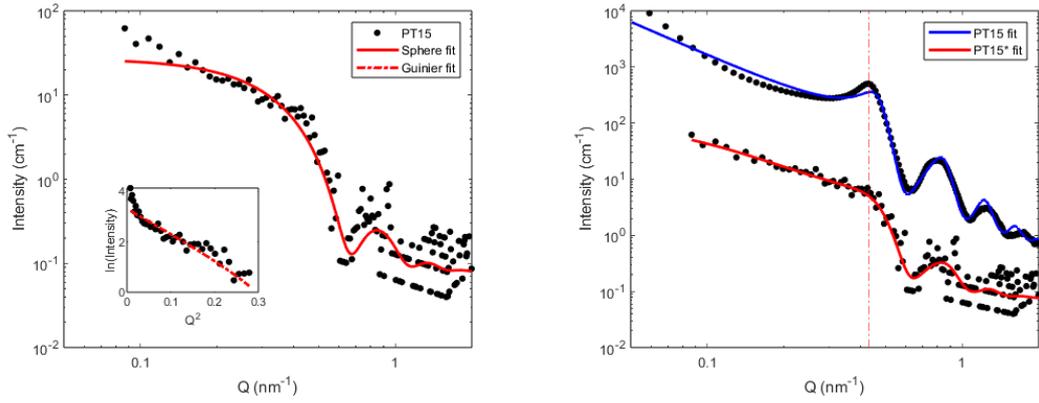(c) Compare between PT20 and T20 samples, SHS fit for both.

(d) Compare between PT15 and T15 samples, SHS fit for both.

Figure 4.13: SAXS data of PT20 and PT15 samples, fitted by sphere and sticky-hardsphere (SHS) model, and Guinier model in low Q range.

4.2.2 SAXS under applied magnetic field

Figure 4.14 shows the SAXS data of PT15* sample obtained from field-assisted SAXS experiments and measured after the magnet was switched off. The particle size and its corresponding spherical fit curve of PT15* sample seem to be more reasonable (see table 4.2.3) than PT15 sample, with no obvious peak around 0.4 nm^{-1} in figure 4.14(b). This suggests that the nanoparticle aggregation observed in the PT15 sample is reversible and could be disrupted by the application of a magnetic field. The reason why the SAXS data of PT15* appear scattered by is due to the time resolution, which was performed over only one minute. As a result, the data were not averaged over a large number of acquisitions, resulting in a lower signal-to-noise ratio.

(a) Sphere and Guinier fit of PT15 sample.   (b) Compare between PT15 and PT15* samples, SHS fit for both.

Figure 4.14: SAXS data of PT15* sample, fitted by sphere and stickyhardsphere (SHS) model, and Guinier model in low Q range.

Samples	R_0(nm)	σ (polydispersity)	$R_g[R_c]$(nm)	R_{eff}(nm)	Vol.	ϵ	τ
PT15*	6.6(2)	7.1(9)%	5.3(7) [6.9(3)]	6.9(8)	1.3(3)%	0.131(2)	0.1

**Table 4.2.3:** Fitting parameters for PT15* sample, R_0 is the spherical radius, σ is the log-normal standard deviation, $R_g[R_c]$ are the gyration radius and correspond spherical radius, R_{eff} is the effective radius of stickyhard sphere, Vol. is the volume fraction, ϵ is the stickiness and τ is the perturbation.

Figure 4.15 shows the SAXS azimuthal distribution of samples T25, T20 and T15

under an applied magnetic field, together with the corresponding intensity evolution over time. In the magnetic field, all three samples show two prominent peaks near ± 90°, indicating an anisotropic structural orientation, probably corresponding to chain-like arrangements of nanoparticles. These peaks gradually disappear after the magnetic field is turned off (around 60s) as shown in the right-hand side of figures 4.15(a), 4.15(b) and 4.15(c). This behaviour suggests that T25, T20 and T15 samples exhibit structural anisotropy under a magnetic field, forming a chain-like structure as shown schematically in Figure 4.16(a). Once the field is removed, the particles revert to a more isotropic scattering profile indicative of random orientation (Figure 4.16(c)).
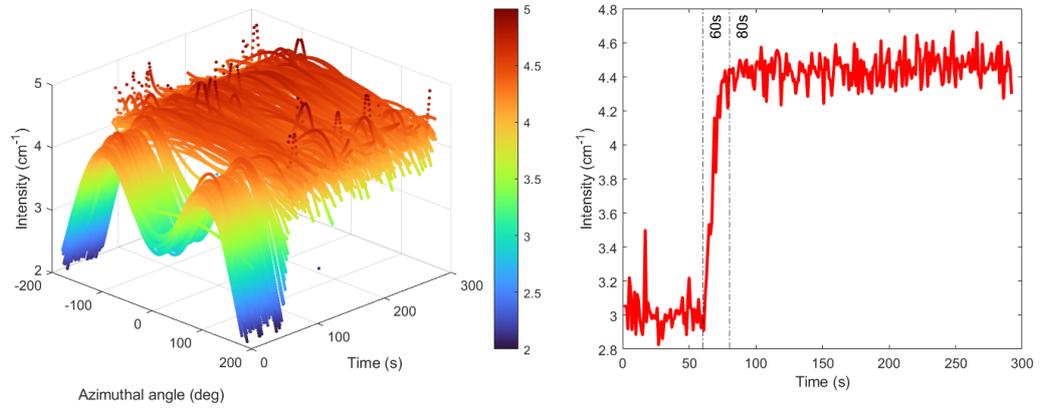
(a) Azimuth distribution of T25 in field and intensity at 0° vs. time
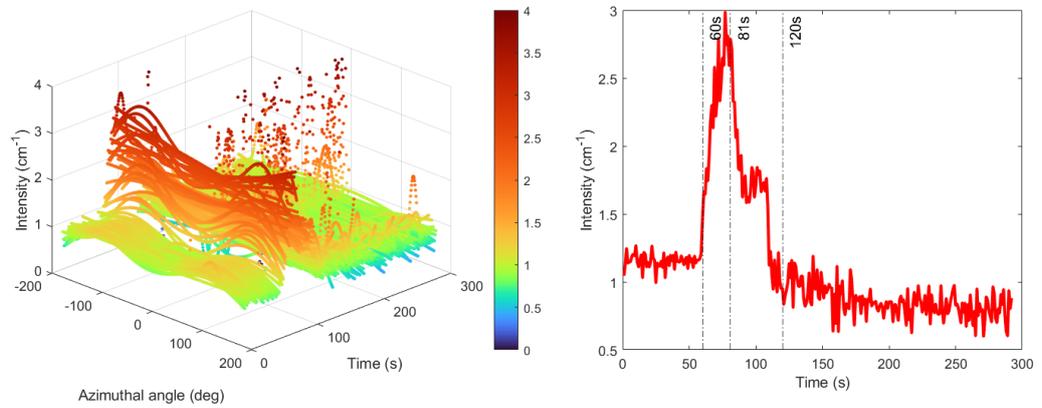
(b) Azimuth distribution of T20 in field and intensity at 90° vs. time
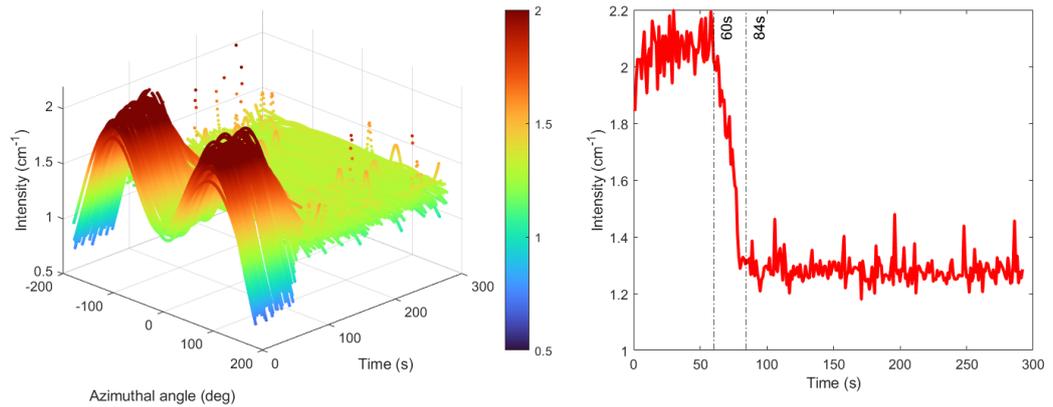
(c) Azimuth distribution of T15 in field and intensity at 90° vs. time

Figure 4.15: Two peaks Gaussian fitted azimuth distribution of T25, T20 and T15, magnetic field is removed at 60 s

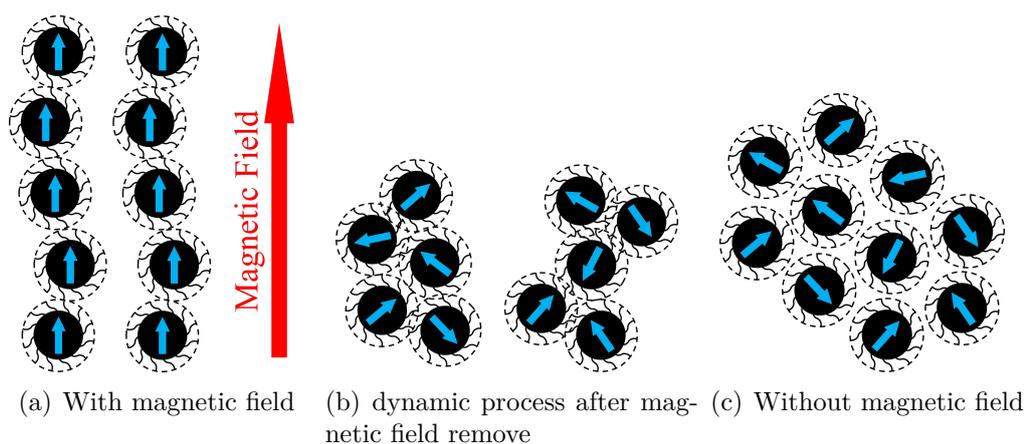(a) With magnetic field   (b) dynamic process after magnetic field remove   (c) Without magnetic field

**Figure 4.16:** Nanoparticles structure of studied samples with and without field

The characteristic time for this structural relaxation, summarised in Table 4.2.4, is approximately 20 seconds for all toluene-based samples. The gradual intensity decrease of T20 between 81 s and 120 s may represent a dynamic stabilisation process where the residual orientation relaxes back to equilibrium (Figure 4.16(b)). As T20 lies between T25 and T15, this intermediate dynamic behaviour may be sample-specific rather than systematic.

Samples	t_1(s)	t_2(s)	Resiudal anisotropy
T25	20	unobserved	no
T20	21	59	no
T15	24	unobserved	no
PT20	24	60	no
PT15	unobserved	68	yes

Table 4.2.4: Summarizing the characteristic structural response times: t_1 is the time at which anisotropy disappears and t_2 is the time range for stabilization.

Figure 4.17 shows the azimuthal SAXS distributions and intensity profiles for PT20 and PT15 samples. In figure 4.17(a), it is clear that PT20 sample undergoes a slower structural change compared to T20 sample, which is in line with expectations due to the presence of PEG 550. Furthermore, Figure 4.17(b) shows a residual anisotropic structure in PT15 sample even after the field is turned off. This unexpected behaviour suggests that the nanoparticles in PT15 sample maintain a partial

chain-like structure in the absence of an external magnetic field. Such residual anisotropy is an unexpected behaviour that may require further investigation, or it may be caused by increased solvent viscosity, which may hinder the disassembly of field-induced structures.
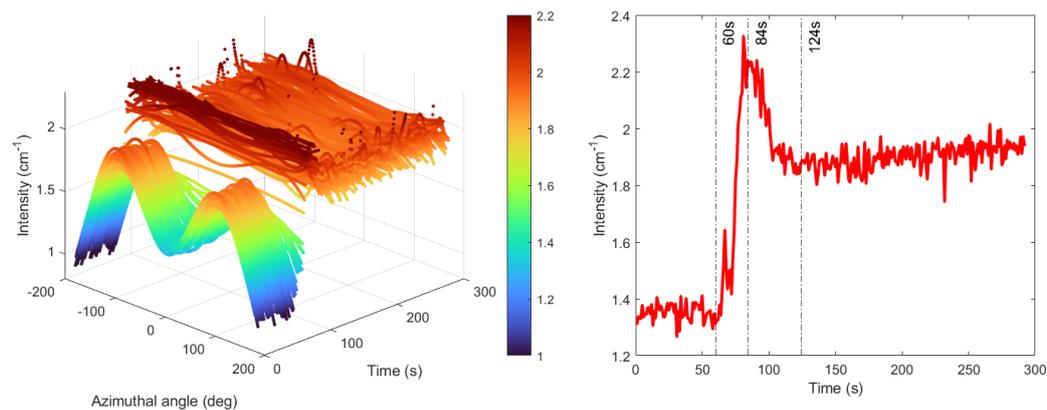
(a) Azimuth distribution of PT20 in field and intensity at 0° vs. time
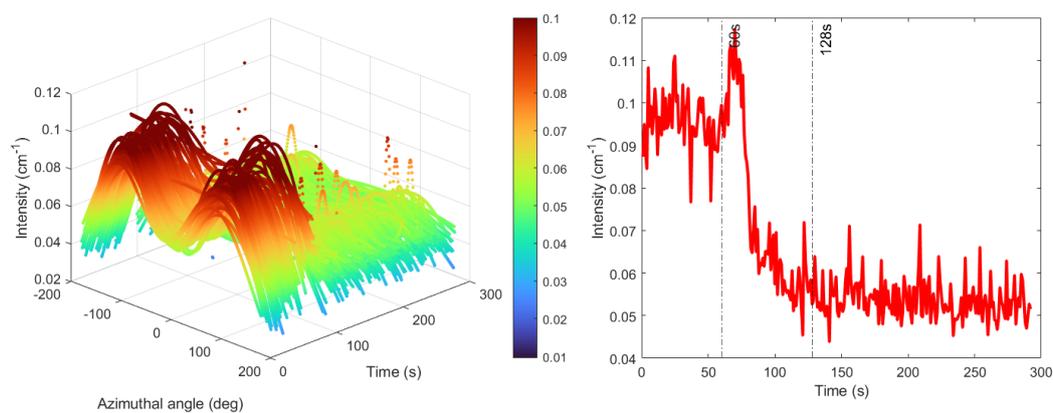
(b) Azimuth distribution of PT15 in field and intensity at 90° vs. time

Figure 4.17: Two peaks Gaussian fitted azimuth distribution of PT20 and PT15, magnetic field is removed at 60 s

4.2.3 DLS

Figure 4.18 shows the DLS results of T$_{DLS}$ sample (10 μg/ml). Measurement A was taken immediately after sample preparation, measurements B and C were taken immediately after measurement A (i.e., A→B→C). The hydrodynamic diameters and corresponding amplitudes are summarized in Table 4.2.5. It is clear from the data that nanoparticle aggregation began immediately after sample preparation. Over time, the particles continued to aggregate into larger aggregates, eventually forming large aggregates with a hydrodynamic diameter of 482 nm by measurement C. This is evident from the increasing count rate during measurement A (see centre of figure 4.18(a)), particularly in the first five minutes, indicating ongoing aggregation. In contrast, the count rates during measurements B and C (Figures 4.18(b) and 4.18(c)) remain approximately stable, indicating that the aggregation formation was complete. The rapid aggregation of the nanoparticles could be due to a decrease in ligand concentration during dilution. Therefore, there were not enough ligands to keep the nanoparticles stable in the solvent. However, it is observed in measurement A that a few nanoparticles with a hydrodynamic diameter of 20 nm are measured. Since the core diameter is known to be around 15 nm, it is reasonable to conclude that the 20 nm measurement represents individual, non-aggregated nanoparticles.

Measurements	$R_{H.1}$(nm)	Amplitude	$R_{H.2}$(nm)	Amplitude
A	20	1.4%	193	98.6%
B	157	4.7%	454	95.3%
C	482	100%		

Table 4.2.5: Hydrodynamic diameters R_H and corresponding amplitudes obtained from DLS measurements of the T$_{DLS}$ sample, the amplitude means percent of particle number.
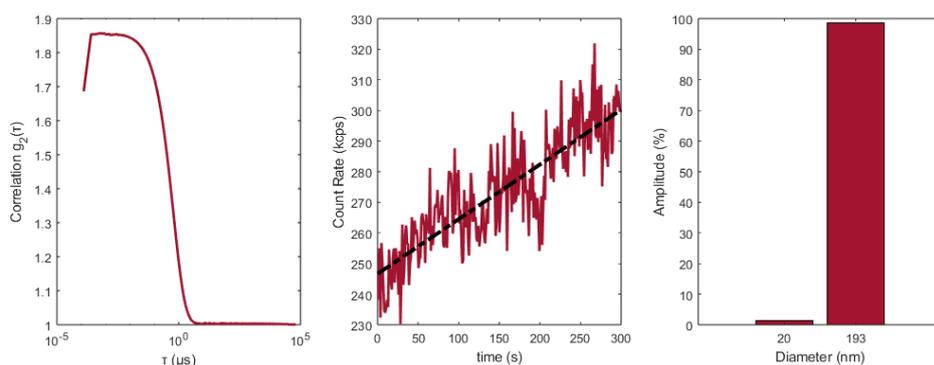
(a) Measurement A
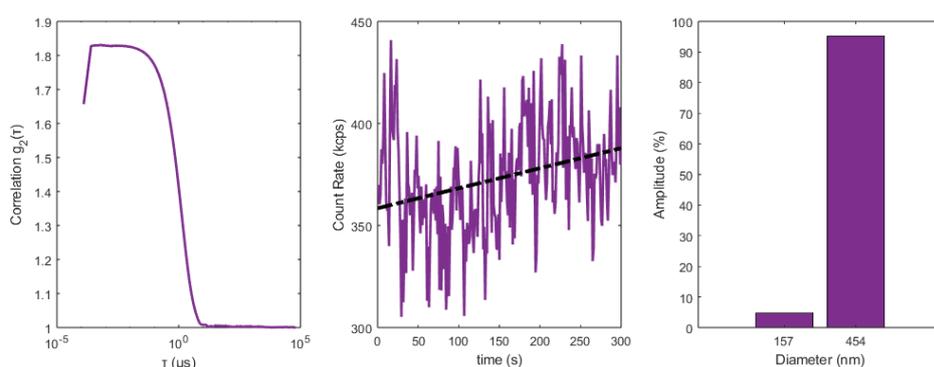
(b) Measurement B
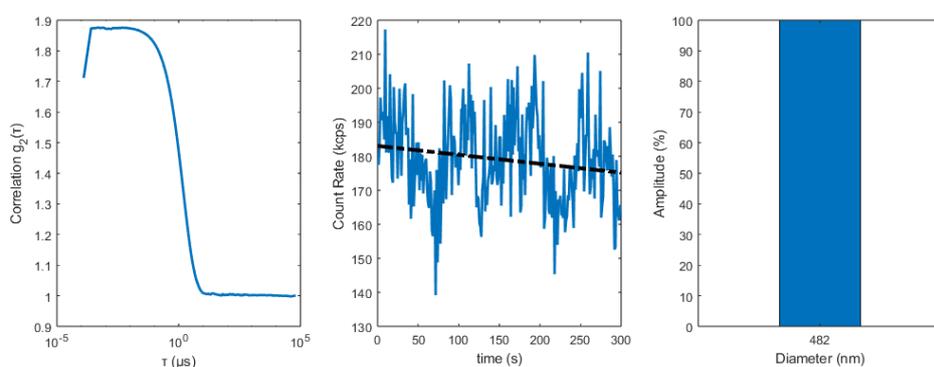
(c) Measurement C

Figure 4.18: Correlation function, count rate, and hydrodynamic radius obtained from DLS measurements: (a) immediately after dilution (Measurement A), and (b, c) Measurements B and C, taken sequentially, show progressive aggregation, with C indicating complete formation of large aggregates.

4.2.4 Summary

In this section, the size and structure of 15 nm iron oxide nanoparticles dispersed in toluene and PEG550/toluene mixture are studied. The core diameter of the nanoparticles is 14.2 nm with a size distribution of 7%, while the hydrodynamic diameter is assumed to be 20 nm. Nanoparticles of T25, T20 and T15 all fit the sticky hard sphere model very well. It is therefore assumed that the effect of dilution is negligible and that there is a short-range attractive interaction between the nanoparticles. Adding PEG 550 (20 and 40%) into toluene does not break this attractive interaction, but 40% PEG 550 changes the solvent environment too much, so the nanoparticles may aggregate slightly, which can be removed by applying a magnetic field. It is also speculated that the nanoparticles form a chain structure in the magnetic field. When the field is removed, the nanoparticles along the chains assemble as aggregates for a short time and then gradually separate. This structural transition of nanoparticles in toluene takes about 20 seconds. This time is increased to 50 seconds by adding 20% PEG 550 to toluene. It is worth noting that 40% PEG 550 in toluene not only prolongs the structural transition time, but also maintains this structural anisotropy for at least another 240 s.

5 Conclusions

Based on the study of 15 nm iron oxide nanoparticles dispersed in toluene and PEG 550/toluene mixture, the dynamic behaviour and structural change of nanoparticles in the magnetic field are characterised.

The magnetic state of the nanoparticle dispersion is strongly influenced by temperature. With decreasing temperature, nanoparticles gradually transition from superparamagnetism to superspin glass behaviour around 160 K, i.e., disordered magnetic moments become spin-glass ordered, while the factor n, which describes the magnetic interaction strength of nanoparticles, is close to the critical value ($n = 1$) for superferromagnetism. The blocking temperature peak in the zero field cooling curve is around 210 K, which is covered by the Brownian relaxation induced peak due to toluene melting (melting point at 180 K for toluene). The contribution of Néel relaxation to magnetic moment alignment can be observed before solvent melting.

The core diameter and hydrodynamic diameter of the nanoparticles are measured to be 14.2 and 20 nm, respectively. There is probably a short-range attractive interaction between the nanoparticles due to van der Waals forces between surface atoms (Fe and O) of nanoparticles and solvent molecules (toluene and PEG 550). Hence, the nanoparticles form a chain structure in the magnetic field. When the magnetic field is removed, the nanoparticles assemble along the chain and then disperse apart. However, this structural transition can be delayed by increasing the viscosity of the solvent, for example by adding PEG550 into toluene.

Therefore, the Brownian and Néel relaxation of magnetic nanoparticles can be distinguished not only by freezing the solvent, but also by changing the viscosity of the solvent. These findings may inform the design of magnetically responsive systems for applications such as targeted drug delivery, magnetic hyperthermia, or contrast-enhanced imaging.

6 Outlook

Overall, this project successfully verifies the feasibility of separating Brownian and Neel relaxation by freezing the solvent and provides an additional approach by modifying the viscosity. However, several results need further investigation, for example the second peak around 280 K in the zero field cooling curve and the bias from the sticky hard sphere model fit in PEG 550/toluene = 40%. Also, the influence of the dilution on nanoparticle ligands should be considered, especially for the sample preparation for dynamic light scattering measurements. Therefore, the use of nanoparticles synthesized directly in our laboratory could eliminate many complications, such as unknown concentrations of ligands as stabilizers, and obtain more flexible choices of the solvent. A standardization of sample preparation for the magnetic properties characterization is necessary because the evaporation of the solvent must be inhibited and the dosage of the dispersion should remain exactly the same in each measurement. In addition, other imaging techniques, such as liquid cell TEM, can be used to more directly observe the structural transition of nanoparticles due to the magnetic field. If a more efficient approach is developed to study single magnetic relaxation in different solvents, the results would directly impact technological applications, e.g., in medical technology. In particular, understanding the influence of solvent viscosity and field-induced structural changes on nanoparticle relaxation dynamics provides a basis for tuning response times, optimising heating efficiency and enhancing imaging contrast. By tailoring the physical environment and magnetic field conditions, such systems could be designed for improved performance in complex biological media, enabling more efficient delivery strategies, localised therapeutic activation or real-time magnetic diagnostics.

7 Acknowledgments

Completing this Master's thesis has been a journey of growth, discovery and profound gratitude. To every person who has walked with me through this endeavour, through moments of triumph and uncertainty, I extend my deepest and most heartfelt appreciation.

First and foremost, I am grateful to **Prof. Dr. Karen Friese (JCNS-2)** for granting me the opportunity to conduct my research at the **Jülich Centre for Neutron Science (JCNS-2)**. Equally, I owe thanks to **Prof. Dr. Regina Dittmann (PGI-7)** for agreeing to serve as my second examiner and for opening the doors of **Peter Grünberg Institute 7 (PGI-7)** institute to provide resources and guidance whenever needed.

To my mentors, **Dr. Asmaa Qdemat (JCNS-2)** and **Priv.-Doz. Dr. Oleg Petracic (JCNS-2)**, I owe immeasurable thanks, not only for your academic guidance but for the humanity you brought to this journey.

Dr. Asmaa Qdemat (JCNS-2), your expertise in X-ray scattering shaped the structural backbone of this work. From deciphering SAXS patterns to modeling nanoparticle interactions, you guided me through the labyrinth of scattering theory with clarity and grace. Your meticulous approach to data analysis taught me the art of balancing rigor with creativity. Most importantly, you showed me how to see beauty in the subtlety of scattering data, a lesson I will carry forward.

Priv.-Doz. Dr. Oleg Petracic (JCNS-2), you opened the door to the world of nanomagnetism. With patience and precision, you taught me to navigate complex instruments like the SQUID magnetometer and PPMS system, transforming theoretical concepts into tangible skills. Beyond the lab, your calm reassurance during moments of uncertainty reminded me that scientific pursuit is as much about resilience as it is about discovery.

Together, you formed an exceptional mentorship team whose collaborative spirit and interdisciplinary guidance helped me overcome both experimental and intellectual

challenges. Your critical feedback and unwavering support, especially during the final stages of writing, ensured the clarity and rigor of my work. Your dedication and belief in my potential inspired me beyond measure.

My sincere thanks extend to **Dr. Martin Dulle (JCNS-1)**, whose expertise transformed my SAXS experiments from daunting challenges into enlightening experiences. Your willingness to pause your research to assist me, coupled with your insightful explanations of scattering principles, profoundly shaped this work. To **Dr. Johan Buitenhuis (IBI-4)**, thank you for patiently demystifying DLS techniques, providing ample solvents, and ensuring my experiments thrived. Your support was indispensable.

I am deeply thankful to **Sascha Ehlert (JCNS-1)**, whose expertise in testing solvents paved the way for successful viscosity adjustments. Without your dedication to identifying PEG550 as the optimal choice, this study would have faltered. To **Maximilian Enneking (JCNS-2)**, your shared wisdom as a fellow student provided clarity during my early steps, and your legacy of kindness continues to inspire. The vibrant community at JCNS-2 deserves special mention. To all colleagues who offered camaraderie, technical advice, or simply a listening ear, thank you for making Jülich feel like a second home. Your collective spirit reminded me that science thrives on collaboration.

Finally, to **my family** and my beloved **Jinhao Zhang (PGI-7)**: you are my anchor. Your unconditional love, patience, and encouragement carried me through sleepless nights and moments of doubt. **Jinhao**, your unwavering belief in me, even when I doubted myself, gave me the courage to persist. This achievement is as much yours as it is mine.

A Appendix

A.1 Pictures

(a) MPMS and PPMS samples
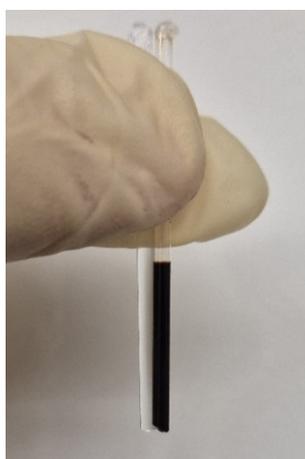
(b) Normal SAXS samples

(c) Field-assisted SAXS samples

(d) DLS sample

Figure A.1: Samples of measurements

(a) MPMS-XL SQUID Magnetometer

(b) PPMS system

Figure A.2: MPMS-XL SQUID Magnetometer and PPMS system

(a) GANESHA
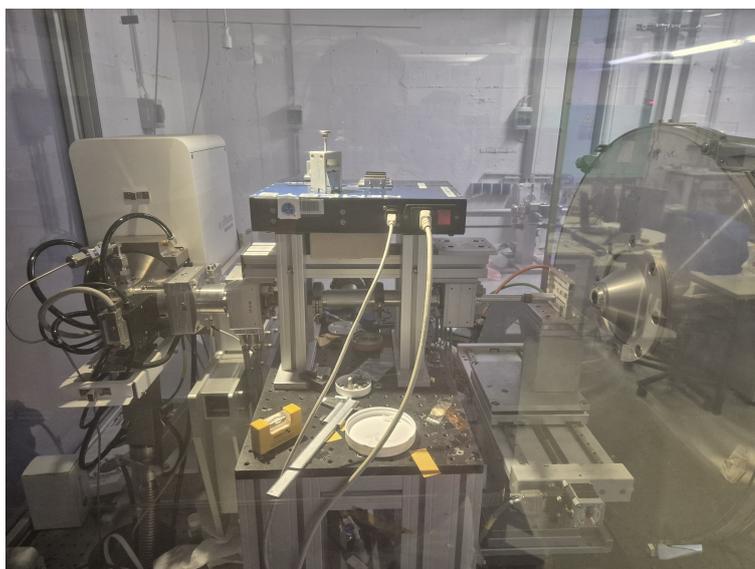
(b) X-ray source

(c) Sample holder for normal SAXS

(d) Sample holder for field-assisted SAXS

Figure A.3: GANESHA X-ray scattering instrument

Figure A.4: ALV/CGS-3 Platform based Goniometer Systems for DLS

A.2 AC-Susceptibility unit conversion

The PPMS system measures AC susceptibility by measuring the slope dM of the magnetic response in emu, which is the *CGS* unit. To convert this into an AC susceptibility of the *SI* unit system, it must be divided by the amplitude dH of the applied external field in Oe and the volume V in cm³. This must then be multiplied by 4π to obtain the AC susceptibility in SI units.

$$\chi_{AC}(SI) = 4\pi\frac{1}{V}\frac{dM}{dH}(CGS) \qquad (A.1)$$

The volume is estimated at 0.481%*10 μm³ here, and 0.481% corresponds to the volume fraction of 25 mg/ml iron oxide nanoparticles dispersion.

B List of Abbreviations

MNPs	Magnetic Nanoparticles
SQUID	Superconducting Quantum Interference Device
PPMS	Physical Property Measurement System
SAXS	Small-Angle X-ray Scattering
DLS	Dynamic Light Scattering
ZFC/FC	Zero-Field Cooling / Field Cooling
SSG	Superspin Glass
SFM	Superferromagnetism
SPM	Superparamagnetism
RKKY	Ruderman-Kittel-Kasuya-Yosida Interaction
PEG	Polyethylene Glycol
MRI	Magnetic Resonance Imaging
TEM	Transmission Electron Microscopy
HS	Hard Sphere Model
SHS	Sticky Hard Sphere Model
MPMS	Magnetic Property Measurement System
ACMS	AC Magnetic Susceptibility Option
CONTIN	Constrained Regularization for Inverse Problems
SLD	Scattering Length Density

C List of Symbols

χ	Magnetic Susceptibility
T_C	Curie Temperature
T_N	Néel Temperature
E_{dd}	Dipolar Interaction Energy
J	Exchange Interaction Constant
J_{RKKY}	RKKY Exchange Integral
K	Anisotropy Constant
K_{eff}	Effective Anisotropy Constant
θ	Angle between Magnetization and Easy Axis
N_x, N_y, N_z	Demagnetization Factors
R_c	Critical Radius for Single Domain
M_s	Saturation Magnetization
τ_N	Néel Relaxation Time
τ_B	Brownian Relaxation Time
τ_{eff}	Effective Relaxation Time
T_b	Blocking Temperature
τ_0	Attempt Time
η	Solvent Viscosity
V_H	Hydrodynamic Volume
$\vec{q}$	Scattering Vector
$I(q)$	Scattering Intensity
$F(q)$	Form Factor
$S(q)$	Structure Factor
R_g	Radius of Gyration

D_f	Diffusion Coefficient
d_h	Hydrodynamic Diameter
χ', χ''	Real / Imaginary Susceptibility
ω	Angular Frequency
ξ	Coherence Factor
M_r	Remanent Magnetization
H_c	Coercive Field
$W(t)$	Magnetic Relaxation Rate
n	Relaxation Exponent
Δm	Relaxation Magnitude
R_{eff}	Effective Radius (SHS Model)
σ	Polydispersity Index
ϵ	Stickiness Parameter
Vol.	Volume Fraction
t_1, t_2	Structural Relaxation Times

Bibliography

[1] S Bayda, M Adeel, T Tuccinardi, M Cordani, and F Rizzolio. The history of nanoscience and nanotechnology: from chemical physical applications to nanomedicine. *Molecules*, 25(1):112, 2019.

[2] K A Altammar. A review on nanoparticles: characteristics, synthesis, applications, and challenges. *Frontiers in microbiology*, 14:1155622, 2023.

[3] S Iravani. Bio-based synthesis of magnetic nanoparticles and their applications. *Magnetic nanostructures: environmental and agricultural applications*, pages 13–31, 2019.

[4] M Modestino, A Galluzzi, F Dinelli, M Sarno, M Polichetti, et al. Study of magnetic interactions in a sample of Fe_3O_4 magnetic nanoparticles in DC and AC fields. *IL NUOVO CIMENTO C*, 47(5):297–1, 2024.

[5] Md E Sadat, S L Bud'ko, R C Ewing, H Xu, G M Pauletti, D B Mast, and D Shi. Effect of dipole interactions on blocking temperature and relaxation dynamics of superparamagnetic iron-oxide (Fe_3O_4) nanoparticle systems. *Materials*, 16(2):496, 2023.

[6] J C Davidson, N R Anderson, and K L Livesey. Field-dependent magnetic relaxation times of magnetic nanoparticle systems: Analytic approximations supported by numerical simulations. *Physical Review B*, 110(14):144447, 2024.

[7] J Seifert, K Koch, M Hess, and A M Schmidt. Magneto-mechanical coupling of single domain particles in soft matter systems. *Physical Sciences Reviews*, 7(11):1237–1261, 2022.

[8] E Roeben, L Roeder, S Teusch, M Effertz, U K Deiters, and A M Schmidt. Magnetic particle nanorheology. *Colloid and Polymer Science*, 292:2013–2023, 2014.

[9] M Hess, M Gratz, H Remmer, S Webers, J Landers, D Borin, F Ludwig, H Wende, S Odenbach, A Tschöpe, et al. Scale-dependent particle diffusivity and apparent viscosity in polymer solutions as probed by dynamic magnetic nanorheology. *Soft Matter*, 16(32):7562–7575, 2020.

[10] C Saayujya, K Yousuf, Y Hao, A Hartley, K H Yeo, A Swamynathan, J Garlepp, Q Huynh, Z W Tay, P Chandrasekharan, et al. Pulsed MPI relaxometry of brownian and néel field-dependent relaxation in superparamagnetic magnetite nanoparticles confirm theory and simulations. *Small*, 20(44):2403283, 2024.

[11] Z Fu, Y Xiao, A Feoktystov, V Pipich, M S Appavou, Y Su, E Feng, W Jin, and T Brückel. Field-induced self-assembly of iron oxide nanoparticles investigated using small-angle neutron scattering. *Nanoscale*, 8(43):18541–18550, 2016.

[12] D Zákutná, D Nižňanskỳ, L C Barnsley, E Babcock, Z Salhi, A Feoktystov, D Honecker, and S Disch. Field dependence of magnetic disorder in nanoparticles. *Physical Review X*, 10(3):031019, 2020.

[13] S Blundell. *Magnetism in condensed matter*. OUP Oxford, 2001.

[14] D Jiles. *Introduction to magnetism and magnetic materials*. CRC press, 2015.

[15] AC Berceanu and M Mostovoy. Ferromagnetic insulator state in doped $FeTiO_3$. 2008.

[16] J Dulińska-Litewka, A Łazarczyk, P Hałubiec, O Szafrański, K Karnas, and A Karewicz. Superparamagnetic iron oxide nanoparticles—current and prospective medical applications. *Materials*, 12(4):617, 2019.

[17] X Batlle and A Labarta. Finite-size effects in fine particles: magnetic and transport properties. *Journal of Physics D: Applied Physics*, 35(6):201, 2002.

[18] O Petracic. Superparamagnetic nanoparticle ensembles. *Superlattices and Mi-*

crostructures, 47(5):569–578, 2010.

[19] D Fiorani, JL Dormann, F Lucari, F D'Orazio, E Tronc, and JP Jolivet. Dynamical magnetic behavior of interacting $\gamma - Fe_2O_3$ particles. *Applied organometallic chemistry*, 12(5):381–386, 1998.

[20] D Fiorani, JL Dormann, R Cherkaoui, E Tronc, F Lucari, F D'orazio, L Spinu, M Nogues, A Garcia, and AM Testa. Collective magnetic state in nanoparticles systems. *Journal of magnetism and magnetic materials*, 196:143–147, 1999.

[21] S Bedanta, X Chen, S Sahoo, W Kleemann, E Kentzinger, P Nordblad, S Cardoso, and PP Freitas. Collective magnetic states of ferromagnetic nanoparticles in the superspin limit. *physica status solidi (c)*, 1(12):3288–3296, 2004.

[22] M Knobel, WC Nunes, LM Socolovsky, E De Biasi, JM Vargas, and JC Denardin. Superparamagnetism and other magnetic features in granular materials: a review on ideal and real systems. *Journal of nanoscience and nanotechnology*, 8(6):2836–2857, 2008.

[23] X Chen, S Bedanta, O Petracic, W Kleemann, S Sahoo, S Cardoso, and PP Freitas. Superparamagnetism versus superspin glass behavior in dilute magnetic nanoparticle systems. *Physical Review B—Condensed Matter and Materials Physics*, 72(21):214436, 2005.

[24] S A Rovers, R Hoogenboom, M F Kemmere, and J TF Keurentjes. Relaxation processes of superparamagnetic iron oxide nanoparticles in liquid and incorporated in poly (methyl methacrylate). *The Journal of Physical Chemistry C*, 112(40):15643–15646, 2008.

[25] R E Rosensweig. Heating magnetic fluid with alternating magnetic field. *Journal of magnetism and magnetic materials*, 252:370–374, 2002.

[26] M Krumrey. Small angle X-ray scattering. In *Characterization of Nanoparticles*, pages 173–183. Elsevier, 2020.

[27] N Stribeck. X-ray scattering of soft matter. 2007.

[28] H Schnablegger and Y Singh. The SAXS guide: getting acquainted with the principles. 2017.

[29] A P Minton. Recent applications of light scattering measurement in the biological and biopharmaceutical sciences. *Analytical biochemistry*, 501:4–22, 2016.

[30] R TC Ju, C W Frank, and A P Gast. Contin analysis of colloidal aggregates. *Langmuir*, 8(9):2165–2171, 1992.

[31] J Lim, S P Yeap, H X Che, and S C Low. Characterization of magnetic nanoparticle by dynamic light scattering. *Nanoscale research letters*, 8:1–14, 2013.

[32] A Nasser, A Qdemat, H Unterweger, R Tietze, X Sun, J Landers, J Kopp, B Wu, M S Appavou, A Murmiliuk, et al. Impact of coating type on structure and magnetic properties of biocompatible iron oxide nanoparticles: insights into cluster organization and oxidation stability. *Physical Chemistry Chemical Physics*, 26(38):24912–24923, 2024.

[33] A G Kolhatkar, A C Jamison, D Litvinov, R C Willson, and T R Lee. Tuning the magnetic properties of nanoparticles. *International journal of molecular sciences*, 14(8):15977–16009, 2013.

[34] O Petracic, X Chen, S Bedanta, W Kleemann, S Sahoo, S Cardoso, and PP Freitas. Collective states of interacting ferromagnetic nanoparticles. *Journal of Magnetism and Magnetic Materials*, 300(1):192–197, 2006.

[35] J Dieckhoff, D Eberbeck, M Schilling, and F Ludwig. Magnetic-field dependence of brownian and néel relaxation times. *Journal of applied physics*, 119(4), 2016.

[36] SasView Project. Sasview version 5.0.6. 2020.

[37] J Nogués and I K Schuller. Exchange bias. *Journal of Magnetism and Magnetic Materials*, 192(2):203–232, 1999.

[38] A Sukhov and J Berakdar. Temperature-dependent magnetization dynamics of magnetic nanoparticles. *Journal of Physics: Condensed Matter*, 20(12):125226,

2008.

[39] T Köhler. Magnetization distribution in superparamagnetic iron oxide nanoparticles. 2022.

[40] M Ulrich, J García-Otero, J Rivas, and A Bunde. Slow relaxation in ferromagnetic nanoparticles: Indication of spin-glass behavior. *Physical Review B*, 67(2):024416, 2003.

[41] X Chen, S Sahoo, W Kleemann, S Cardoso, and PP Freitas. Universal and scaled relaxation of interacting magnetic nanoparticles. *Physical Review B—Condensed Matter and Materials Physics*, 70(17):172411, 2004.

[42] A Guinier, G Fournet, C B Walker, and G H Vineyard. Small-angle scattering of X-rays, 1956.